

Formation of strong fronts in the 2-D quasigeostrophic thermal active scalar

Peter Constantin[†], Andrew J Majda^{†§} and Esteban Tabak[§]

[†] Department of Mathematics, University of Chicago, Chicago, IL 60637, USA

[†] Department of Mathematics, Princeton University, Princeton, NJ 08544, USA

[§] Programm in Applied and Computational Mathematics, Princeton University, Princeton, NJ 08544, USA

Received 15 July 1994

Recommended by R Krasny

Abstract. The formation of strong and potentially singular fronts in a two-dimensional quasigeostrophic active scalar is studied here through the symbiotic interaction of mathematical theory and numerical experiments. This active scalar represents the temperature evolving on the two dimensional boundary of a rapidly rotating half space with small Rossby and Ekman numbers and constant potential vorticity. The possibility of frontogenesis within this approximation is an important issue in the context of geophysical flows. A striking mathematical and physical analogy is developed here between the structure and formation of singular solutions of this quasigeostrophic active scalar in two dimensions and the potential formation of finite time singular solutions for the 3-D Euler equations. Detailed mathematical criteria are developed as diagnostics for self-consistent numerical calculations indicating strong front formation. These self-consistent numerical calculations demonstrate the necessity of nontrivial topology involving hyperbolic saddle points in the level sets of the active scalar in order to have singular behaviour; this numerical evidence is strongly supported by mathematical theorems which utilize the nonlinear structure of specific singular integrals in special geometric configurations to demonstrate the important role of nontrivial topology in the formation of singular solutions.

AMS classification scheme numbers: 76L05, 35L65, 35B40, 35A40

1. Introduction

We study the detailed nonlinear behaviour of strong and potentially singular front formation in solutions of a two-dimensional quasi-geostrophic active scalar through the symbiotic interaction of mathematical theory and numerical experiments. Our motivation for this study is generated from two distinct sources. One motivation involves actual geophysical flows in the atmosphere and the important issue of frontogenesis, the formation of strong fronts between masses of hot and cold air, within quasigeostrophic approximations without explicitly incorporating ageostrophic effects [1]. Frontogenesis is the terminology used by atmosphere scientists for describing the formation in finite time of a discontinuous temperature front. The second motivation, developed in detail in section 2 of this paper, is the striking physical and mathematical analogy between the behaviour of strongly nonlinear solutions of these equations in two dimensions and the behaviour of potentially singular solutions for the Euler equations of 3-D incompressible flow [2] — an outstanding unsolved problem in the theoretical turbulence community. In this second instance, the problem studied here in two dimensions is simpler than 3-D Euler, both numerically and analytically,

yet retains a large number of crucial features which are analogous to the behaviour in 3-D Euler.

The equations studied here are given by

$$\frac{D\theta}{Dt} = \frac{\partial\theta}{\partial t} + v \cdot \nabla\theta = 0 \quad (1.1)$$

where the two-dimensional velocity, $v = (v_1, v_2)$ is determined from θ by a stream function

$$(v_1, v_2) = \left(-\frac{\partial\psi}{\partial x_2}, \frac{\partial\psi}{\partial x_1} \right) \quad (1.2)$$

and the stream function ψ satisfies

$$(-\Delta)^{\frac{1}{2}} \psi = -\theta. \quad (1.3)$$

With $x = (x_1, x_2)$, the nonlocal operator $(-\Delta)^{\frac{1}{2}}$, in (1.3) is determined through the Fourier transform

$$\psi(x) = \int e^{2\pi i x \cdot k} \hat{\psi}(k) dk$$

by

$$(-\Delta)^{\frac{1}{2}} \psi = \int e^{2\pi i x \cdot k} 2\pi |k| \hat{\psi}(k) dk. \quad (1.4)$$

We comment briefly on the derivation of the nonlinear equations in (1.1)–(1.3). The variable θ represents the potential temperature, v is the fluid velocity, and the stream function ψ can be identified with the pressure. These equations are derived from the more general quasigeostrophic approximation [1] for nonhomogeneous fluid flow in a rapidly rotating three-dimensional half-space with small Rossby and Ekman numbers; for the case of special solutions with constant potential vorticity in the interior and constant buoyancy frequency (normalized to one), the general quasigeostrophic equations reduce to the evolution equations for the temperature on the two-dimensional boundary given in (1.1)–(1.3). The statistical turbulence theory for these special quasigeostrophic flows has been studied earlier by Blumen [3] and more recently by Pierrehumbert *et al* [4] while some qualitative features of the solutions of these equations in a geophysical context are developed by Held *et al* [5]. The equations in (1.1)–(1.3) are an important example of a two-dimensional active scalar [6], the *thermal quasigeostrophic active scalar*, with a specific structure most closely related to the 3-D Euler equations (see section 2). A brief preliminary study of potential singular solutions for these equations has been developed recently by the authors [7]. Next we present an outline of the remainder of this paper.

In section 2, we develop the striking physical and mathematical analogies between the quasigeostrophic active scalar in (1.1)–(1.3) and the 3-D Euler equations for incompressible flow. One simple physical example of this analogy in section 2 is that level sets of solutions of the quasigeostrophic active scalar correspond to vortex lines in the 3-D Euler equations—both types of curves move with the flow and the nonlocal equation for evolution of the tangent vectors to the level sets is completely analogous to the equation of vortex stretching for the vorticity, which is tangent to vortex lines. This mathematical analogy is also exploited in section 2 where the authors develop precise mathematical criteria to characterize

the fashion in which smooth solutions of the equations in (1.1)–(1.3) can become singular. The simplest result of this type is the analogue of the well known characterization for singular solutions for 3-D Euler in [8], namely,

$[0, T_*)$ with $T_* < \infty$ is a maximal interval of existence of a smooth solution for the 2-D quasigeostrophic active scalar if and only if

$$\int_0^T |\nabla\theta|_{L^\infty}(s) ds \rightarrow \infty \text{ as } T \nearrow T_* \quad (1.5)$$

where $|f|_{L^\infty} = \max_{x \in \mathbb{R}^2} |f(x)|$. More refined criteria of this sort involving the rate of increase of the length of level sets for the active scalar are also developed in section 2.

In section 3, numerical experiments are presented where the refined mathematical criteria developed in section 2 are utilized as diagnostics for self-consistent numerical solutions predicting strong front formation and potentially singular behaviour in a sequence of calculations with finer resolution ranging from 256^2 to 512^2 to 1024^2 with a pseudo-spectral method and periodic boundary conditions. Three types of initial data are considered in section 3. The first experiments involve a hyperbolic saddle in the initial level sets of temperature in the regime of strong nonlinear behaviour—the numerical solutions indicate strong nonlinear front formation and potentially singular behaviour. The second series of experiments involves initial data which globally is very similar to that in the first set of experiments, but the geometry in the vicinity of the strongest nonlinear region is different and involves elliptic level sets in θ —the numerical solutions in this case initially behave nonlinearly as in the first set of experiments but self-consistently saturate to exponential growth of gradients without singular behaviour. Finally, in the third set of experiments reported in section 3, more general initial data is considered which indicates the robust features of strong front formation documented in the numerical experiments reported earlier in the section.

The first two series of numerical experiments from section 3 demonstrate the important role of the geometry of the level sets of the active scalar in strongly nonlinear and potentially singular behaviour. In section 4, such a geometric scenario is developed in detail once again through the symbiotic interaction of mathematical theory and numerical experiments. In particular, mathematical theorems for solutions of the quasigeostrophic active scalar are stated in section 4 with the following basic theme: *if the geometry of the level sets of the active scalar is simple and does not contain a hyperbolic saddle in the region of strongly nonlinear behaviour, then no singular behaviour is possible.* In particular, the mathematical theory necessarily implies that no fronts with simple regular level set topology in the temperature field, θ , can become singular in finite time. In other words, classical frontogenesis i.e., the finite time development of a shock-like discontinuous thermal front, is impossible for solutions of the quasigeostrophic active scalar, but as documented in section 3, strong nonlinear front formation with a nontrivial hyperbolic saddle in the θ level sets is possible within the quasigeostrophic approximation. More data from the two numerical experiments in section 3 involving the role of geometry and strongly nonlinear behaviour are also presented in section 4; these data corroborate the mathematical theory presented earlier in section 4.

The proofs of the mathematical results from section 4 are given in section 5. These proofs utilize the nonlinear structure of specific singular integrals acting on functions in special geometric configurations. Similar results for the 3-D Euler equations have been

announced in [6] and will appear in a forthcoming paper of C Fefferman and two of the authors [9]. The mathematical theory presented below is for all of space while the numerical simulations involve periodic geometry. We do not repeat the analogous theoretical results in a periodic setting since the proofs are somewhat easier but leave them as a simple exercise for the interested reader.

2. Analogies between the 2-D quasigeostrophic active scalar and the 3-D Euler equations

The 3-D incompressible Euler equations in vorticity-stream form [2, 6] are given by

$$\frac{D\omega}{Dt} = (\nabla v)\omega \quad (2.1)$$

where $\frac{D}{Dt} = \frac{\partial}{\partial t} + v \cdot \nabla$, $v = (v_1, v_2, v_3)$ is the three-dimensional velocity field with $\text{div } v = 0$, and $\omega = \text{curl } v$ is the vorticity vector.

We begin our list of physical, geometric, and analytic analogies between the 2-D quasigeostrophic active (QG) scalar in (1.1)–(1.3) and the 3-D Euler equations from (2.1) by introducing

$$\nabla^\perp \theta = (-\theta_{x_2}, \theta_{x_1}) \quad (2.2)$$

We claim that the vector field, $\nabla^\perp \theta$, has a role for the 2-D QG active scalar in (1.1)–(1.3) completely analogous to the vorticity in 3-D incompressible fluid flow, i.e.

$$\nabla^\perp \theta \longleftrightarrow \omega \quad (2.3)$$

By differentiating the equation in (1.1), we obtain the evolution equation for $\nabla^\perp \theta$ given by

$$\frac{D\nabla^\perp \theta}{Dt} = (\nabla v)\nabla^\perp \theta \quad (2.4)$$

with $\frac{D}{Dt} = \frac{\partial}{\partial t} + v \cdot \nabla$ and $v = \nabla^\perp \psi$ so that $\text{div } v = 0$. With the identification in (2.3), the evolution equation in (2.4) for $\nabla^\perp \theta$ clearly has, at the outset, a similar superficial structure resembling the equation for vorticity in (2.1). Next we show that this analogy extends considerably beyond this superficial level to detailed analytic and geometric properties of solutions.

2.1. The analytic analogy with vortex stretching

We begin by demonstrating that the equations in (2.1) and (2.4) are remarkably similar in their analytic structure. The velocity v in (2.1) is determined from the vorticity ω by the familiar Biot–Savart law [2, 6],

$$v(x) = -\frac{1}{4\pi} \int_{R^3} \left(\nabla^\perp \frac{1}{|y|} \right) \times \omega(x+y) dy \quad (2.5)$$

and the strain matrix, S , which is the symmetric part of the velocity gradient,

$$S = \frac{1}{2} ((\nabla v) + (\nabla v)^*)$$

is given in terms of the vorticity by the strongly singular integral,

$$S(x) = \frac{3}{4\pi} P.V. \int_{R^3} M(\hat{y}, \omega(x+y)) \frac{dy}{|y|^3} \tag{2.6}$$

In (2.6) the matrix M is a function of two variables, the first a unit vector, the second a vector and is given by the formula

$$M(\hat{y}, \omega) = \frac{1}{2} [\hat{y} \otimes (\hat{y} \times \omega) + (\hat{y} \times \omega) \otimes \hat{y}] \tag{2.7}$$

with $a \otimes b = (a_i b_j)$ the matrix formed by the tensor product of two vectors. Clearly the right hand side of (2.1) can be written in terms of only the strain matrix, S , and ω . For the 2-D QG active scalar, the equations in (1.3) and (1.4) are given through the explicit integral formula

$$\psi(x) = - \int_{R^2} \frac{1}{|y|} \theta(x+y) dy \tag{2.8}$$

so that with $v = \nabla^\perp \psi$, we obtain

$$v = - \int_{R^2} \frac{1}{|y|} \nabla^\perp \theta(x+y) dy \tag{2.9}$$

Next, we compute the symmetric part of the matrix, ∇v , from (2.4) defined by

$$S(x) = \frac{1}{2} (\nabla v + (\nabla v)^*)$$

With (2.9) we calculate that the matrix $S(x)$ has the singular integral representation

$$S(x) = P.V. \int_{R^2} N(\hat{y}, (\nabla^\perp \theta)(x+y)) \frac{dy}{|y|^2} \tag{2.10}$$

where $\hat{y} = \frac{y}{|y|}$ and N is a function of two variables, the first a unit vector in R^2 and the second a vector with

$$N(\hat{y}, \omega) = \frac{1}{2} (\hat{y}^\perp \otimes \omega + \omega \otimes \hat{y}^\perp) \tag{2.11}$$

The function N has mean zero on the unit circle for fixed ω and thus, the operator in (2.10) is a legitimate strongly singular integral. As in the situation for 3-D fluid flow, we will see below that for the equation in (2.4), only the symmetric part, $S(x)$, contributes to strong and potentially singular front formation. We have displayed only the formula for the symmetric part of ∇v for simplicity in the exposition.

With the formulae in (2.5)–(2.11), we develop the analytic analogy between the equations in (2.1) and (2.4). From (2.5) and (2.9), the velocity is given in terms of w , either ω or $\nabla^\perp \theta$ respectively in 3-D or 2-D, by

$$v = \int_{R^d} K_d(y) w(x+y) dy$$

where $K_d(y)$ is homogeneous of degree $1-d$ in R^d for $d = 2, 3$, i.e. $K_d(\lambda y) = \lambda^{1-d} K_d(y)$ for $\lambda > 0$. Furthermore, from (2.7) and (2.10)

$$\frac{\nabla v + (\nabla v)^*}{2} = S(x)$$

has a representation formula in terms of $w(x+y)$ via a strongly singular integral operator defined through a kernel homogeneous of degree $-d$, in R^d , for $d = 2, 3$ with specific cancellation properties; also the geometric formulae for these strongly singular operators given in (2.7) and (2.11) are very similar in structure. Thus, with the identification of $\nabla^\perp \theta$ and vorticity, the evolution equation for $\nabla^\perp \theta$ from (2.4) has a completely parallel analytic structure in 2-D as the equation for the evolution of vorticity, ω , in (2.1) for 3-D incompressible flow.

2.2. The geometric analogy with vortex lines

The analogy in (2.3) extends much farther beyond the detailed analytic structure in (2.1) and (2.4). From (1.1) it follows that the level sets, $\theta = \text{constant}$, move with the fluid flow and $\nabla^\perp \theta$ is tangent to these level sets; these facts are analogues for the 2-D QG active scalar of the well-known facts for 3-D incompressible fluid flow that the vorticity by definition is tangent to vortex lines and vortex lines move with the fluid. Thus,

$$\begin{aligned} &\text{for the 2-D QG active scalar, the level sets of} \\ &\theta \text{ are analogous to vortex lines for 3-D Euler.} \end{aligned} \quad (2.12)$$

The infinitesimal length of a vortex line is given by the magnitude of ω , $|\omega|$, and it follows readily from (2.1) (see [6]) that the evolution of this infinitesimal length is given by

$$\frac{D|\omega|}{Dt} = \alpha|\omega| \quad (2.13)$$

with

$$\alpha(x, t) = S(x, t)\xi \cdot \xi. \quad (2.14)$$

Here $S(x, t)$ is the symmetric matrix defined in and above (2.6) and $\xi(x, t)$ is the unit direction of the vorticity vector, i.e. $\xi = \frac{\omega(x, t)}{|\omega(x, t)|}$. Similarly, for the 2-D QG active scalar the infinitesimal length of a level set for θ is given by $|\nabla^\perp \theta|$ and from (2.4), the evolution equation for the infinitesimal arc length is given by

$$\frac{D|\nabla^\perp \theta|}{Dt} = \alpha|\nabla^\perp \theta| \quad (2.15)$$

with

$$\alpha(x, t) = S(x, t)\xi \cdot \xi. \quad (2.16)$$

Here $S(x, t)$ is the symmetric matrix defined in and above (2.10) and $\xi(x, t)$ is the unit direction of $\nabla^\perp \theta$, i.e. $\xi = \frac{\nabla^\perp \theta}{|\nabla^\perp \theta|}$. With the analogy in (2.12) between level sets for the 2-D QG active scalar and vortex lines, the similar equations in (2.13) and (2.15) and also the parallel formulae in (2.6) and (2.10) for the stretching factor α , it should be evident to the reader that there is a powerful geometric-analytic analogy between these two problems in 2-D and 3-D respectively.

2.3. Conserved quantities

The 2-D QG active scalar in (1.1)–(1.3) obviously has the quantities conserved in time for solutions given by

$$\int_{R^2} G(\theta) dx \quad (2.17)$$

for any function $G(\theta)$. With the Fourier transform defined in (1.4), it follows that $\widehat{v}(k) = \widehat{\nabla^\perp \psi}(k) = \frac{i(-k_2, k_1)}{|k|} \widehat{\theta}(k)$ so that by Plancherel's formula,

$$\frac{1}{2} \int_{R^2} |v|^2 dx = \frac{1}{2} \int_{R^2} |\theta|^2 dx. \quad (2.18)$$

The facts in (2.17) with the special choice $G(\theta) = \frac{1}{2}\theta^2$ combined with (2.18) establishes the conservation of kinetic energy for the 2-D QG active scalar. This conservation of energy is analogous to that for the 3-D Euler equations.

However, there are additional quantities conserved in time for the 2-D QG active scalar beyond the kinetic energy—for example, all of the quantities listed in (2.17). In addition, the reader can verify readily that the quantity

$$H(\theta) = - \int_{R^2} \psi \theta dx = \int_{R^2} \left((-\Delta)^{-\frac{1}{2}} \theta \right) \theta dx \tag{2.19}$$

is conserved by solutions of the QG active scalar. This is an additional positive definite conserved quantity without a direct analogue for the 3-D Euler equations. Other more geometric conserved quantities for the QG active scalar are presented in section 2.5 below.

2.4. Analogies and the characterization of singular solutions for the 2-D QG active scalar

One of the main themes of this paper is the use of the 2-D QG active scalar as a simpler but analogous model problem for formation of singularities for the 3-D incompressible Euler equations. Here we develop precise mathematical criteria which characterize the fashion in which smooth solutions of the equations in (1.1)–(1.3) can become singular in finite time. These precise mathematical criteria are used as self-consistent diagnostics for numerical experiments in section 3 of this paper; furthermore, these conditions are analogous to similar results [2, 6, 8, 9] for the 3-D Euler equations.

We utilize the Sobolev spaces of functions in $H^S(R^2)$ so that f belongs to $H^S(R^2)$ for a positive integer S if the following norm is finite:

$$|f|_S^2 = \sum_{|\alpha| \leq S} \int_{R^2} |D^\alpha f|^2 dx . \tag{2.20}$$

It is not difficult to prove a local existence theorem for solutions of (1.1) – (1.3) in a standard fashion and to obtain the following result (see chapter 2 of [10] for this type of proof which in this case, is left as an exercise for the interested reader):

If the initial value $\theta|_{t=0} = \theta_0(x)$ belongs to the Sobolev space, $H^k(R^2)$ for some integer $k, k \geq 3$, there is a smooth solution $\theta(x, t)$ of the 2-D QG active scalar belonging to $H^k(R^2)$ for each time, t , in a sufficiently small time interval, $0 \leq t < T_*$. Furthermore, if T_* , the maximal interval of smooth existence is finite, i.e. $T_* < \infty$, then T_* is characterized by the property that

$$\|\theta(\cdot, t)\|_k \rightarrow \infty \text{ as } t \nearrow T_* . \tag{2.21}$$

With this preliminary information, it is not difficult to prove the following precise characterization of the fashion in which smooth solutions of the 2-D QG active scalar can become singular in finite time:

Theorem 2.1. Consider the unique smooth solution of the 2-D QG active scalar with initial data, $\theta_0(x) \in H^k(\mathbb{R}^2)$ with $k \geq 3$. The following are equivalent:

- (1) The time interval, $0 \leq t < T_*$, with $T_* < \infty$ is a maximal interval of H^k existence for the 2-D QG active scalar.
- (2) The quantity $|\nabla^\perp \theta|_{L^\infty}(t)$ accumulates so rapidly that

$$\int_0^T |\nabla \theta|_{L^\infty}(s) ds \rightarrow \infty \quad \text{as } T \nearrow T_* \tag{2.22}$$

- (3) Let $\alpha^*(t) = \max_{x \in \mathbb{R}^2} (S\xi \cdot \xi) = \max_{x \in \mathbb{R}^2} \alpha(x, t)$ where S and α are defined in (2.10), (2.15), (2.16), then

$$\int_0^T \alpha^*(s) ds \rightarrow \infty \quad \text{as } T \nearrow T_* \tag{2.23}$$

In particular, if either of the quantities in (2.22) or (2.23) remains finite as $t \nearrow T_*$ the solution remains smooth beyond the time T_* .

Proof of theorem 2.1. With the analogy between $\nabla^\perp \theta$ and vorticity ω , we see that the fact that (1) and (2) are equivalent is the analogue of the well-known criterion established in [8]; in fact, with the equation in (2.4) and the analogous formulae in (2.9) and (2.10) for v and ∇v in terms of $\nabla^\perp \theta$ for the QG active scalar, the proof that (1) is equivalent to (2) requires only minor changes in the argument from [8]; this is left for the interested reader to verify. It remains to establish that (3) is equivalent to (1). With the fact that $\hat{v}(k) = \frac{i(-k_2, k_1)}{|k|} \hat{\theta}(k)$ and Sobolev's lemma we have the estimates,

$$\begin{aligned} \alpha^*(t) &\leq C |\nabla v|_{L^\infty(\mathbb{R}^2)}(t) \leq C \|\nabla v\|_{k-1}(t) \\ &\leq C \|v\|_k(t) = C \|\theta\|_k(t) \end{aligned} \tag{2.24}$$

for any fixed $k \geq 3$ where C in (2.24) is an a priori constant varying from inequality to inequality. Therefore if we assume (2.23), it follows from integrating the inequality in (2.24) that

$$\int_0^T \|\theta\|_k(s) ds \rightarrow \infty \quad \text{as } T \rightarrow T_*$$

so that $[0, T_*)$ with $T_* < \infty$ is a maximal interval of smooth existence for $\theta(x, t)$. To complete the proof of theorem 2.1, we utilize the fact that 1) and 2) are equivalent and prove that if we assume that

$$\int_0^{T_*} \alpha^*(s) ds \leq M < \infty$$

then necessarily

$$\int_0^{T_*} |\nabla^\perp \theta|_{L^\infty}(s) ds \leq e^M |\nabla^\perp \theta_0|_{L^\infty} < \infty \tag{2.25}$$

The identity in (2.15) for the rate of change of arc length along level sets together with Gronwall's inequality and the definition of α^* in 3) above guarantee that

$$\frac{d}{dt} |\nabla^\perp \theta|_{L^\infty}(t) \leq \alpha^*(t) |\nabla^\perp \theta|_{L^\infty}(t) \tag{2.26}$$

By integrating (2.26) we deduce the estimate claimed earlier in (2.25). This completes our sketch of the proof of theorem 2.1.

There is a refined criterion beyond that in (3) of theorem 2.1 which yields a useful additional diagnostic for the numerical simulations described in the next sections. To state this criterion, we consider the simplified situation where by hypothesis there is an isolated absolute maximum for $|\nabla^\perp \theta|$ achieved along a smooth curve $x(t)$ for $0 < t < T_*$, i.e.,

$$|\nabla \theta|_{L^\infty}(t) = |\nabla^\perp \theta|(x(t), t) . \tag{2.27}$$

There might be several such isolated global maxima but for simplicity we consider only one of them. We consider the level set stretching rate α , defined in (2.15), (2.16), restricted to this curve where $|\nabla \theta|$ is a maximum i.e. we define $\tilde{\alpha}(t)$ by

$$\tilde{\alpha}(t) = \alpha(x(t), t) . \tag{2.28}$$

Intuitively, we expect that no singular behaviour can occur in the solution of the QG active scalar on the interval $[0, T_*)$ unless $\tilde{\alpha}(t) \rightarrow \infty$ as $t \nearrow T_*$. This expectation is confirmed by the following

Proposition 2.1. With the additional geometric hypothesis described in (2.27), the three conditions in theorem 2.1 are equivalent to the (apparently weaker) condition that

$$\int_0^T \tilde{\alpha}(t) dt \nearrow \infty \text{ as } T \nearrow T_* . \tag{2.29}$$

The proof of proposition 2.1 is simple. Since $\tilde{\alpha}(t)$ satisfies $\tilde{\alpha}(t) \leq \alpha^*(t)$, if (2.29) is valid it follows that necessarily (2.23) is valid. On the other hand, assume that

$$\int_0^{T_*} \tilde{\alpha}(t) dt \leq M . \tag{2.30}$$

Let q denote the Lagrangian marker at $t = 0$ associated with the particle trajectory equation so that

$$\begin{aligned} \frac{dX}{dt}(q, t) &= v(X(q, t), t) \\ X(q, t)|_{t=0} &= q . \end{aligned} \tag{2.31}$$

In Lagrangian coordinates, the formula from (2.15) becomes

$$\frac{\partial}{\partial t} |\nabla_x^\perp \theta|(q, t) = \alpha(X(q, t), t) |\nabla_x^\perp \theta|(q, t) \tag{2.32}$$

where $|\nabla_x^\perp \theta|(q, t) = |\nabla^\perp \theta|(X(q, t), t)$. Under the hypothesis in (2.27) and with $q(t)$ defined by $X(q(t), t) = x(t)$

$$\begin{aligned} \frac{d}{dt} |\nabla^\perp \theta|_{L^\infty}(t) &= \frac{d}{dt} (|\nabla_x^\perp \theta|(q(t), t)) = \left(\frac{d}{dt} |\nabla_x^\perp \theta| \right) |_{(q(t), t)} + (\nabla_q |\nabla_x^\perp \theta|) |_{(q(t), t)} \cdot \frac{dq}{dt} \\ &= \left(\frac{d}{dt} |\nabla_x^\perp \theta| \right) |_{(q(t), t)} = \tilde{\alpha}(t) |\nabla_x^\perp \theta|_{L^\infty}(t) . \end{aligned} \tag{2.33}$$

In the third equality in (2.33), we utilized the fact that $|\nabla_x^\perp \theta|$ has a maximum in q at $q(t)$ while we used (2.32) in the fourth equality. With (2.30) and (2.33), we achieve the *a priori* bound in (2.25). This completes the proof of proposition 2.1.

Remark 2.1. We utilize proposition 2.1 in the numerical sections of this paper where the additional hypothesis from (2.27) is satisfied empirically. With a more lengthy proof, the same result remains true without the hypothesis in proposition 2.1. We omit this proof here.

Remark 2.2. The perceptive reader will note that analogous refined criteria for singular solutions for the 3-D Euler equations are valid, as given in (3) of theorem 2.1 and also proposition 2.1, with virtually the identical proofs utilizing (2.13), (2.14) rather than (2.15), (2.16). Since we discuss the 2-D QG active scalar in this paper, we have chosen to emphasize the analogous criteria for that equation here. In the context of the 3-D Euler equations, the proof which we have presented for (3) of theorem 2.1 constitutes a substantial refinement with a vastly simpler proof of a result of Ponce [11] which followed the ideas from [8] and characterized the potential singular solutions of 3-D Euler through the blow up of the strain matrix.

2.5. Theoretical predictions for strong front formation in the QG active scalar

Recently, one of the authors (see [6] and references therein) has derived and applied interesting equations for the convective derivative of the direction field ξ where $\xi = \frac{\omega}{|\omega|}$ for 3-D Euler and $\xi = \frac{\nabla^\perp \theta}{|\nabla^\perp \theta|}$ for any active scalar. In particular, if $\kappa = (\xi \cdot \nabla \xi) \cdot \xi^\perp$ denotes the curvature of a level set of an active scalar, one identity developed on page 89 of [6] is the following:

$$\frac{D}{Dt} (\kappa |\nabla^\perp \theta|) = (\nabla^\perp \theta \cdot \nabla) q \tag{2.34}$$

where $q = ((\nabla v)\xi) \cdot \xi^\perp$.

The integral of $\kappa |\nabla^\perp \theta|$ on a closed level set of θ is the rotation number of that level set. If we integrate the quantity, $\kappa |\nabla^\perp \theta|$, between two level sets, from (2.34), we obtain a *geometric constant of motion which is completely different from those discussed earlier in 2.3*; this constant is the ‘sum’ of the rotation numbers of the level sets contained in the region. Thus, by integrating (2.34), over such a region, we obtain that

$$\frac{d}{dt} \int_{\{x | C_1 \leq \theta(x,t) \leq C_2\}} \kappa |\nabla^\perp \theta| dx = 0 . \tag{2.35}$$

We can use these conserved quantities in (2.35) to make a prediction about the geometric nature of strongly nonlinear regions in solutions for the QG active scalar. In such strongly nonlinear regions, according to theorem 2.1, we necessarily have $|\nabla^\perp \theta| \gg 1$. Thus,

under the hypothesis that the curvature does not oscillate wildly, it follows from the conserved quantities in (2.35) that necessarily the curvature satisfies $|\kappa| \ll 1$, i.e. (2.36)

necessarily straightening of the level sets must occur.

This theoretical prediction is confirmed in all the numerical experiments presented next in section 3 where we always observe general level set flattening in θ in the regions with the most nonlinear behaviour where $|\nabla^\perp \theta|$ is largest and changing most rapidly. It is worth emphasizing again that such a straightening effect of level sets applies to any 2-D active scalar in regions of high gradients provided that the curvature does not oscillate wildly. Wild oscillation could occur with the quantity in (2.35) remaining conserved if locally the curvature, κ , behaved like $f\left(x, t, \frac{x}{\epsilon(t)}\right)$ where $\epsilon(t)$ tends rapidly to zero as t increases. In all of our numerical experiments, we find no evidence for such oscillations.

3. Numerical simulations with strong front formation in the QG active scalar

Here we present the results of systematic numerical simulations for solutions of the QG active scalar together with detailed numerical diagnostics involving the theoretical criteria developed in theorem 2.1 and proposition 2.1—these diagnostics are used both as self-consistent checks of the numerical solutions under refinement and also to monitor the self-consistent potential for singularity formation in a given initial data. We report on numerical simulations with three different initial data here: the first yields strong front formation as predicted theoretically in (2.36) and continued nonlinear development toward a potential singular solution; the second initial data, with a different topology for the θ - level sets, has temporal behaviour with front formation as predicted in (2.36) which saturates rapidly to mildly nonlinear and non-singular behaviour on the time interval computed here. Connections between the topology of θ -level sets and potential singular behaviour confirming these different numerical results are developed in section 4 of this paper. Finally, a third more general initial data is utilized to demonstrate the robustness of flattening of level sets associated with strong gradients as predicted theoretically in (2.36).

3.1. The basic numerical method and diagnostics

We solved the equations in (1.1)–(1.3) numerically on a 2π -periodic box with a spectral collocation method, which involves computing $v(\theta)$ in Fourier space and the product $v \cdot \nabla\theta$ in physical space, with an exponential filter of high frequencies, and time stepping through a fourth-order Runge–Kutta method. This numerical method is basically the one developed by E and Shu [12, 13] for incompressible flow with minor modifications to incorporate the change in physics in (1.1)–(1.3). As a numerical check on the accuracy of the basic scheme and the time stepping procedure, we monitored the two positive definite conserved quantities described in section 2.3 involving the kinetic energy (see (2.18)) and the pseudo energy, $H(\theta)$ (see (2.19)). In the simulations reported below, these quantities were conserved to five significant figures. As diagnostics for the resolution with various numbers of Fourier modes ranging from $(256)^2$ and $(512)^2$ to $(1024)^2$, we monitored the angular averaged energy spectrum. The diagnostics in theorem 2.1 and proposition 2.1 for potential singular behaviour were implemented through straightforward evaluation involving post-processing of the numerical solution.

3.2. Case 1: strong and potentially singular front formation with a hyperbolic saddle in the active scalar topology

In this first case, we considered the simplest initial data with

$$\theta(x, 0) = \sin(x_1) \sin(x_2) + \cos(x_2) . \quad (3.1)$$

Eigenmodes of the Laplacian define temperature fields which are steady solutions of (1.1)–(1.3). The initial data in (3.1) is a linear combination of the two lowest eigenmodes and represents the simplest type of smooth initial data with nonlinear behaviour.

In figure 1, we present the numerical solution with this initial data at the times, $t = 0, 2, 4, 6$ with a resolution of $(512)^2$ Fourier modes. The initial data for the temperature field, $\theta_0(x)$, clearly has a hyperbolic saddle and the numerical solution develops a strong front as time evolves. We are interested in determining whether the front depicted at time $t = 6$ is well-resolved with this method and also whether the numerical solution, resolved on a finer mesh, continues to develop nonlinear and potentially singular structure as time

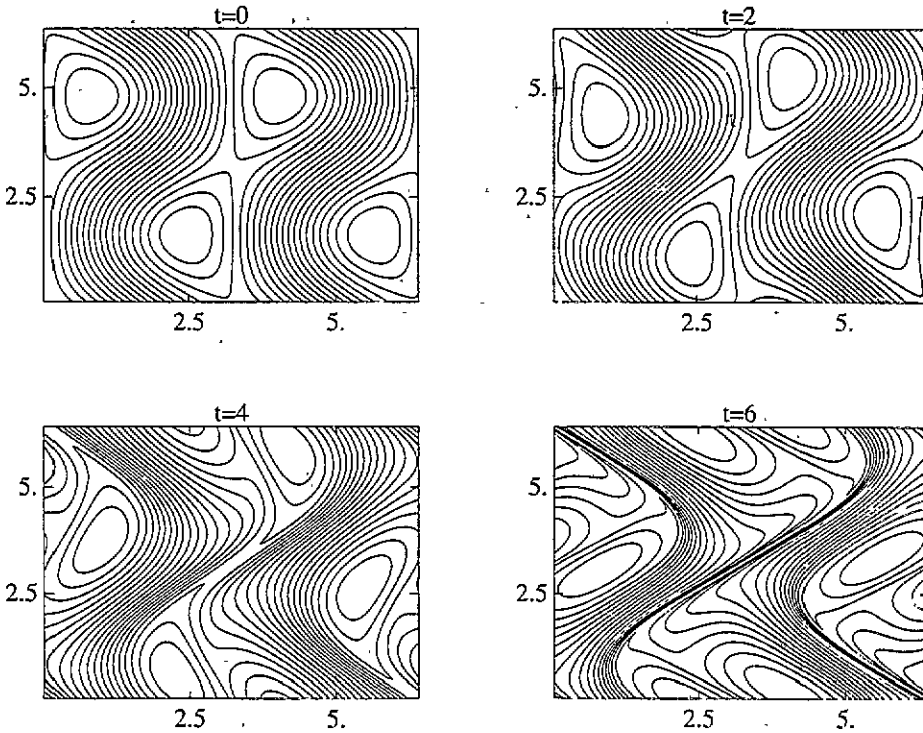


Figure 1. Case 1. Evolution of θ and ψ between $t = 0$ and $t = 6$, exhibiting the initial stages in the development of strong, potentially singular fronts. Both θ and ψ have saddle points at the centre of the grid. (a) Contours of θ . (b) Contours of ψ .

evolves. To determine the numerical resolution, we give plots of the energy spectrum in figure 2 at time, $t = 6$, with $(512)^2$ Fourier modes and also the same plots at times $t = 7$ and $t = 7.5$ with the higher resolution, $(1024)^2$ modes.

These three plots indicate a progressive build up of energy in the higher modes, characterized by an evolving bump in the spectrum. The graph in figure 2(a) indicates that at time $t = 6$, we are near the limit of resolution with $(512)^2$ Fourier modes while figures 2(b, c) demonstrate that we reach the limit of resolution with $(1024)^2$ modes near $t = 7.5$ but have adequate resolution until that time.

In figures 3–5 we plot the level sets of the temperature field and the stream function, ψ , for the velocity field at the times $t = 6, 7, 7.5$ with the numerical resolution of the preceding paragraph. It is evident from these graphs that the transfer of energy to high wave numbers depicted in figure 2 is associated with the nearly self-similar development of a strong temperature front with a cusp. This cusp is clearly displayed at time $t = 6$ in figure 6 where a three-dimensional local graph of θ is presented.

To present further evidence for the roughly self-similar behaviour of the cusped thermal front, in figures 3–5, we have marked the spatial locations where $|\nabla^{\perp}\theta|$ and the stretching factor $\alpha(x, t)$ from (2.15) and theorem 2.1 achieve their maxima; clearly, they are converging to the centre of the hyperbolic saddle in the θ -level sets as time evolves.

Is the roughly self-similar steepening of the cusped thermal front associated with a strongly nonlinear and potentially singular event for the 2-D quasigeostrophic active scalar? Here we utilize theorem 2.1 and proposition 2.1 as refined diagnostics to provide insight

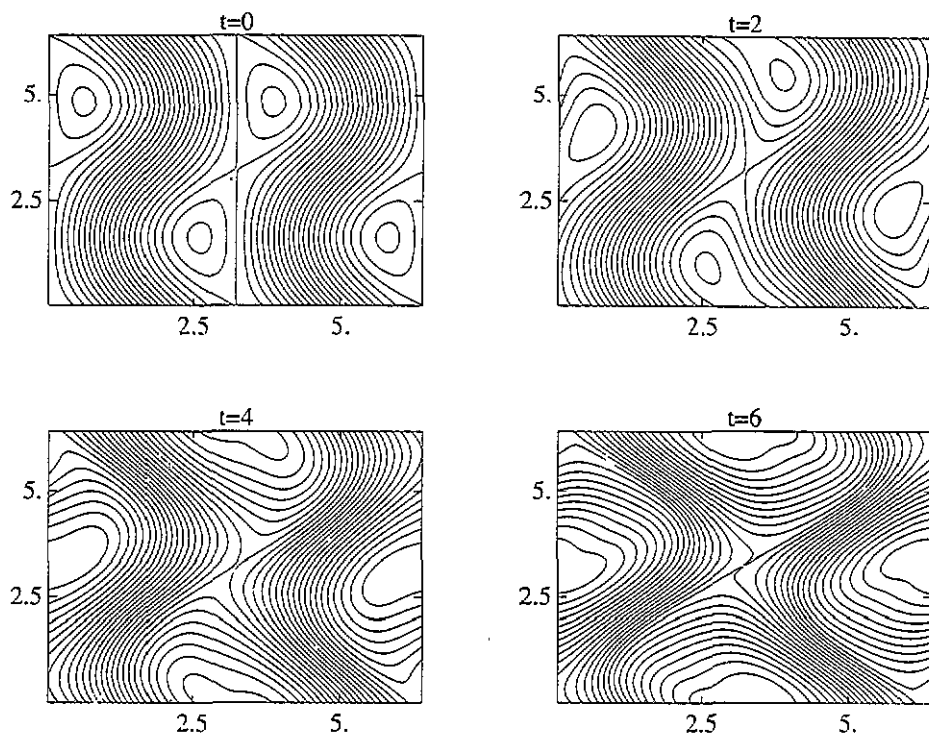


Figure 1. (Continued)

into this basic issue. In figure 7 we present log-log plots of $\max |\nabla^\perp \theta|$ versus time for three different numerical simulations with resolutions of $(256)^2$, $(512)^2$, and $(1024)^2$.

As indicated in figure 7, all three curves agree until the time, $t = 5.5$, where the calculation with $(256)^2$ modes has lost resolution; self-consistently, the calculation with $(512)^2$ modes agrees with the finer resolution calculation until roughly time $t = 6$ where adequate resolution with $(512)^2$ modes has been lost (recall figure 2a). The best linear fit of the curve in figure 7 yields a slope of -1.66 and a potential blow up time T_* , with value roughly, $T_* \cong 8.25$, i.e., a singular behaviour for $|\nabla^\perp \theta|$ like $(T_* - t)^{-1.66}$; these values for a potential singularity are consistent with the requirements of rigorous theory from (2) of theorem 2.1.

In figure 8, we plot $\alpha^*(t)$, the maximum of the stretching factor over the entire periodic box defined earlier in (3) of theorem 2.1, and also $\tilde{\alpha}(t)$, the value of the stretching factor at the location of the maximum for $|\nabla^\perp \theta|$ with $(1024)^2$ modes. According to (3) of theorem 2.1 and proposition 2.1, nonlinear growth in either $\alpha^*(t)$ or $\alpha(t)$ is a signature of strongly nonlinear interaction and growth of gradients (far beyond constant exponential growth!) and divergent behaviour in time for both of these quantities is the signature of a singular solution. First, we discuss the graph of $\alpha^*(t)$; the quantity $\alpha^*(t)$ reflects the global rate of increase of arc length of level sets; the graph of $\alpha^*(t)$ is roughly constant until the time $t = 7$, and $\alpha^*(t)$ exhibits strongly nonlinear growth after $t = 7$. The quantity $\tilde{\alpha}(t)$ gives a more accurate measure of the local nonlinearity in the system at the location of the largest gradient; the behaviour of $\tilde{\alpha}(t)$ is strongly nonlinear until the time $t = 7$; beyond $t = 7$, the curve $\tilde{\alpha}(t)$ lies below $\alpha^*(t)$. According to the data presented in figures 3–5, the locations of the maximum of α yielding $\alpha^*(t)$ and the location of the maximum magnitude for the

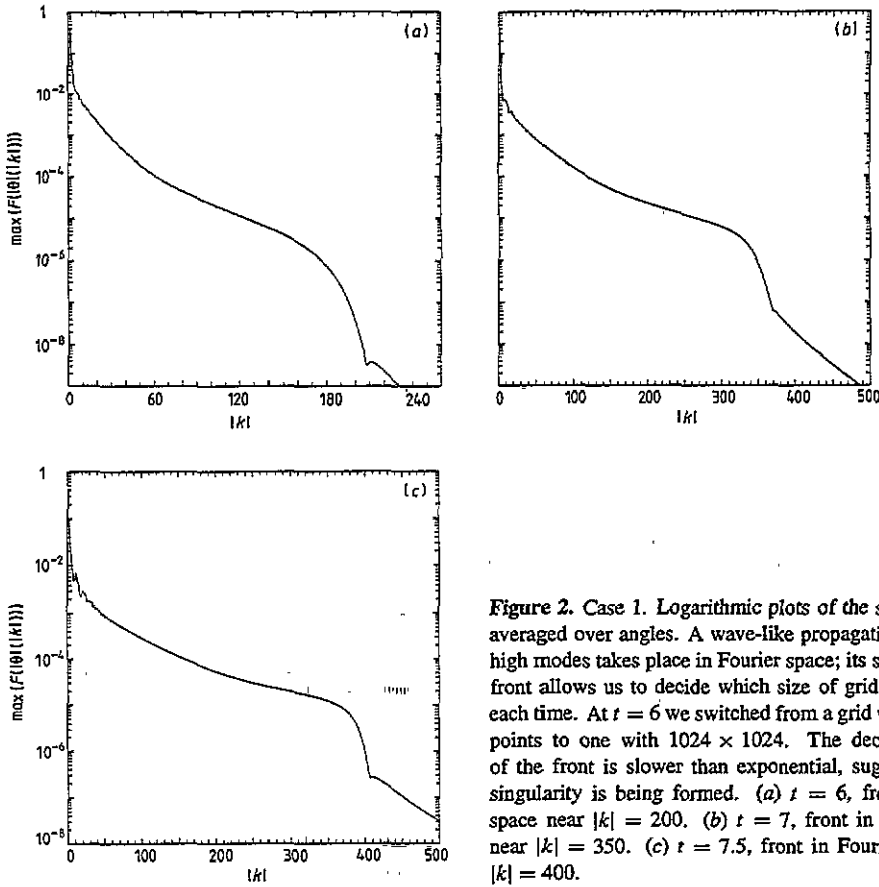


Figure 2. Case 1. Logarithmic plots of the spectrum of θ , averaged over angles. A wave-like propagation toward the high modes takes place in Fourier space; its sharply defined front allows us to decide which size of grid is required at each time. At $t = 6$ we switched from a grid with 512×512 points to one with 1024×1024 . The decay to the left of the front is slower than exponential, suggesting that a singularity is being formed. (a) $t = 6$, front in Fourier space near $|k| = 200$. (b) $t = 7$, front in Fourier space near $|k| = 350$. (c) $t = 7.5$, front in Fourier space near $|k| = 400$.

gradient yielding $\tilde{\alpha}(t)$ converge rapidly and nearly coincide around the time, $t = 7$. In the regime with $7 \leq t \leq 7.5$, near the limits of resolution on a fixed mesh (see figure 2) with strong nonlinear growth, the maximum gradient of the actual solution is probably lying between mesh points. Thus, with this rough reasoning, beyond the time, $t = 7$, we take the maximum of the two curves in figure 8 as a measure of the nonlinearity in the system. Thus, this second refined set of mathematical diagnostics indicates continued nonlinear growth consistent with the behaviour presented earlier in figure 7.

To summarize, we have presented numerical evidence, consistent with refined mathematical diagnostics for strongly nonlinear and potentially singular behaviour of the solution of (1.1)–(1.3) with the initial data in (3.1). While the strongly nonlinear behaviour of this cusped thermal front has been established, caution is needed regarding the potential finite time singularity in such a front—even with a resolution of $(1024)^2$ on a Cray C90 supercomputer, from figure 7, we see that the value of the gradient has only amplified by a factor of 30 by the time, $t = 7.5$ where resolution is lost. Obviously, there is a need for a carefully designed new adaptive numerical method to give additional insight. With the theoretical results in [8, 11], mathematical diagnostics for potential singular solutions for the 3-D Euler equations predicted by numerical methods have been used since that time; a review of these efforts until 1991 is presented in [2] and very interesting high quality numerical simulations which systematically utilize such diagnostics in different contexts are presented in [13–15]. Our use of the refined diagnostics involving $\alpha^*(t)$ and $\tilde{\alpha}(t)$ from

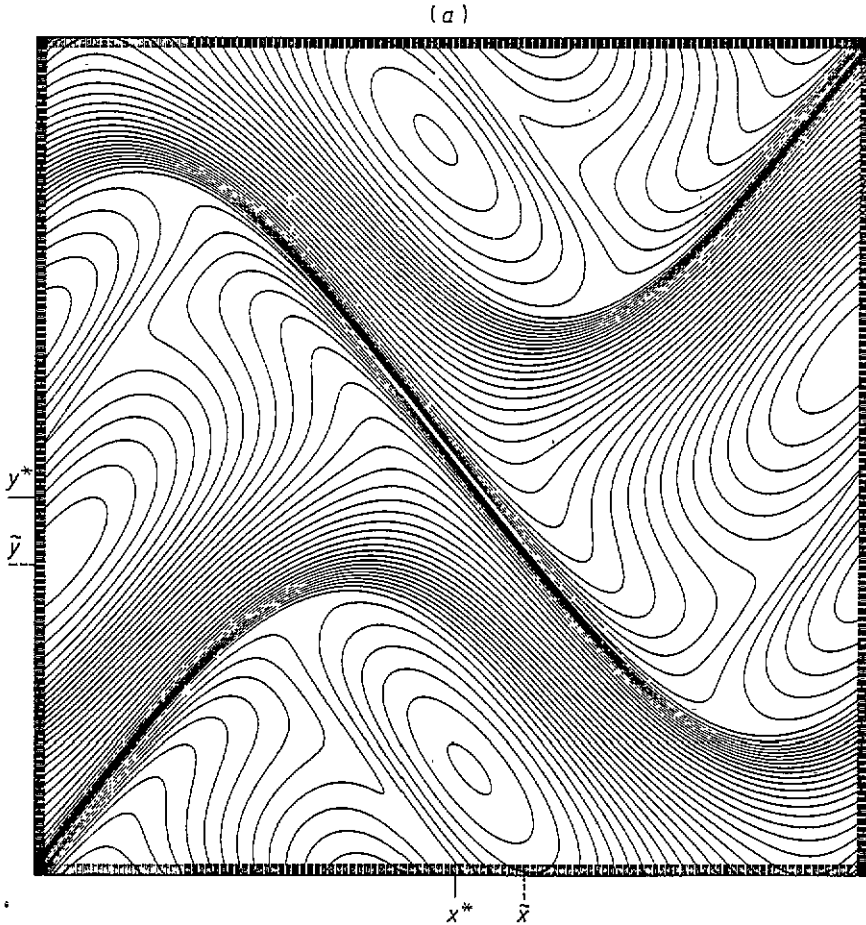


Figure 3. Case 1. Contours of θ and ψ at $t = 6$. From about this time on, the formation of the front follows a seemingly self-similar pattern. (a) Contours of θ , where we have marked the location of maximum $|\nabla\theta|$ (denoted ' \sim ') and maximum strain α (denoted '*'). (b) Contours of ψ .

theorem 2.1 and proposition 2.1 is the first attempt to utilize the most refined mathematical diagnostics in a numerical study.

3.3. Case 2: Nonsingular front formation with an elliptic centre in the active scalar topology

Here we present the results of numerical simulations with the simple initial data given by

$$\theta(x, 0) = -(\cos(2x_1) \cos(x_2) + \sin(x_1) \sin(x_2)) \tag{3.2}$$

In figure 9, we present snapshots of the θ -level sets of the numerical solutions at the times $t = 0, 1.5, 3.0,$ and 4.5 with a resolution of $(512)^2$ Fourier modes. As in case 1 and according to the theoretical prediction in section 2.5, a strong front with nearly planar level sets develops in time. In contrast to case 1 described earlier, the strong front forms in the vicinity of an elliptic centre in the θ -level sets rather than a hyperbolic saddle. We will present further numerical evidence below that the behaviour associated with the solution in case 2 is not strongly nonlinear and far from singular behaviour for this interval of time. In sections 4 and 5, we will present mathematical evidence supporting these numerical results,

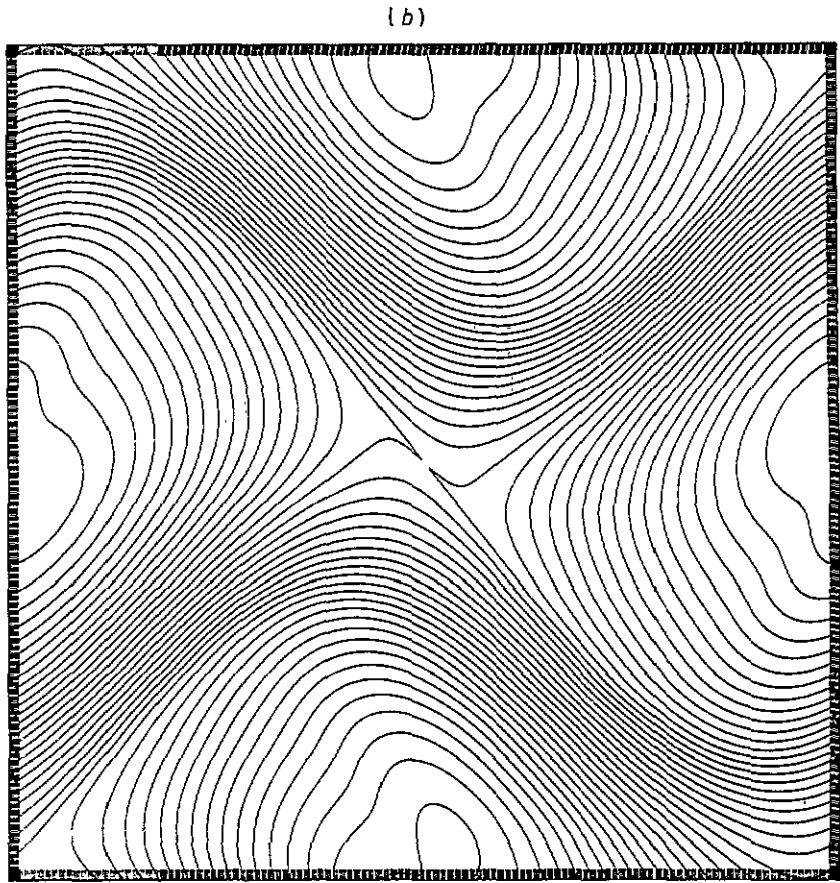


Figure 3. (Continued)

In figure 10 we present the spectrum at time $t = 4$ with $(512)^2$ modes and at time $t = 5$ with $(1024)^2$ modes. figure 10 indicates adequate numerical resolution at these times. These graphs also reveal a transfer of energy to high wave numbers in case 2 but, in contrast to the data presented in figure 2 for case 1, the amplitudes are slightly smaller and the pronounced bump in the spectrum is absent.

In figures 11(a) and 11(b) we give contour plots for the active scalar, θ , at the times, $t = 4$, and $t = 5$ with the numerical resolution described above. Also on these graphs are marked the spatial locations of the maximum of $|\nabla^\perp \theta|$ and the maximum of the stretching factor, α^* . In contrast to the results in figures 3–5 for case 1, these locations remain distinctly separated as time evolves. This behaviour suggests that the strong front that has formed in case 2 is not a strongly nonlinear event as time evolves. In figure 12, we plot $\log(|\nabla^\perp \theta|_{L^\infty})$ as a function of time for $0 \leq t \leq 5$ —as indicated in figure 10(b), we are at the limits of resolution with $(1024)^2$ modes at time $t = 5$.

The graph in figure 12 has a pronounced constant slope for times, t , with $3.75 \leq t \leq 5$. According to the mathematical criterion in (2) of theorem 2.1, this constant slope is the signature of mildly nonlinear exponential growth of the magnitude of $|\nabla^\perp \theta|$ in contrast to case 1 and this is very far from singular behaviour. In figure 13 we graph the temporal behaviour of the quantities $\alpha^*(t)$ and $\bar{\alpha}(t)$ utilized in the refined diagnostics in (3) of theorem

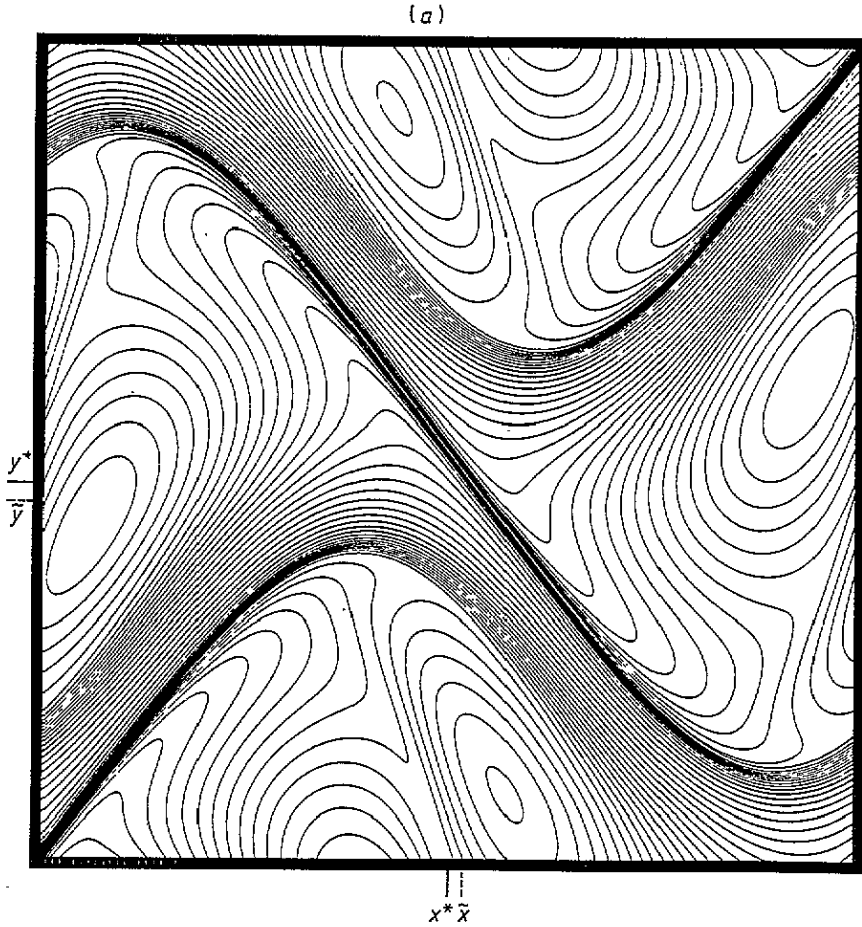


Figure 4. Same as previous figure, at $t = 7$. Observe how the location of the points with maximum gradient and strain have nearly converged to the centre of the grid. (a) Contours of θ . (b) Contours of ψ

2.1 and proposition 2.1. Both of these quantities exhibit mild growth through their history and the more sensitive diagnostic for strongly nonlinear behaviour in the vicinity of the maximum gradient, $\tilde{\alpha}(t)$, is leveling off and is nearly flat for t with $3.75 < t < 5.00$.

Thus, all of the mathematical diagnostics presented in figures 12 and 13 provide self-consistent evidence that the front formation depicted in figures 9 and 11 is only mildly nonlinear and very far from a potentially singular event. Mathematical evidence giving further support for this behaviour is presented in section 4. Here in section 3.3, we have utilized the mathematical diagnostics from theorem 2.1 and proposition 2.1 together with numerical experiments to exclude strongly nonlinear and potentially singular behaviour in a certain geometric configuration for the level sets of the active scalar—despite the fact that visually a strong front has formed.

3.4. Case 3: front formation with general initial data

Here we briefly present the results of our numerical simulations with the more general initial data,

$$\theta(x, 0) = \cos(2x_1) \cos x_2 + \sin x_1 \sin x_2 + \cos(2x_1) \sin(3x_2) . \tag{3.3}$$

(b)

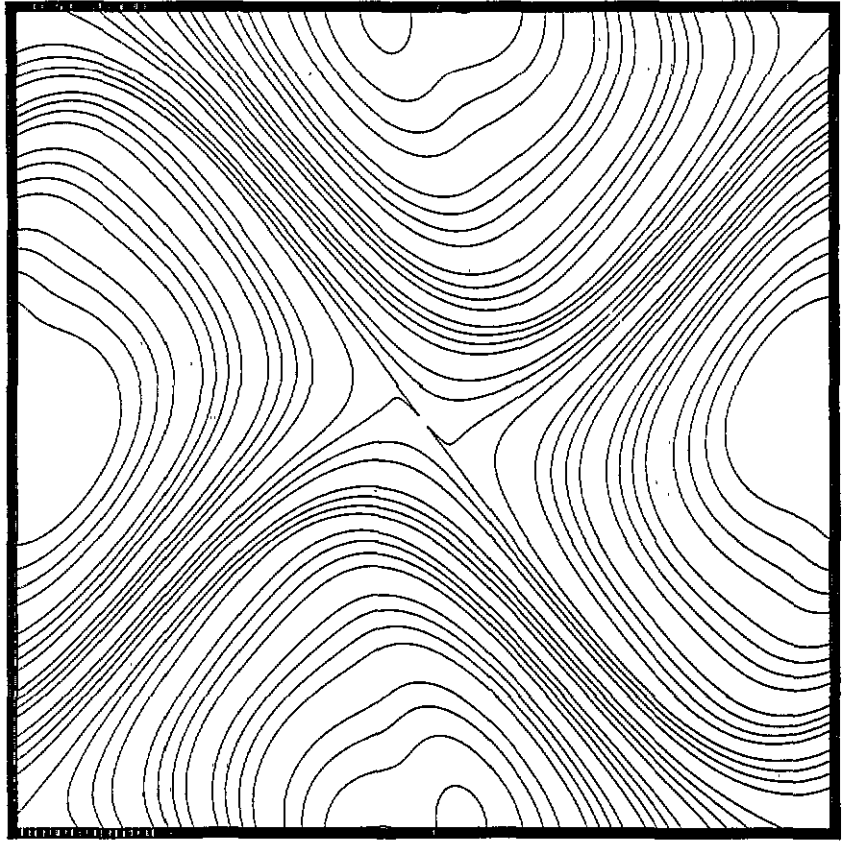


Figure 4. (Continued)

In figures 14 and 15 we present graphs with the active scalar level sets in a numerical simulation with $(1024)^2$ Fourier modes at the times $t = 0$ and $t = 3$ respectively. These plots clearly indicate that the large scale straightening of level sets in regions with large gradients is occurring with this general initial data. This confirms once again, our theoretical prediction from (2.36).

4. The topology of level sets for the active scalar and strong front formation

Cases 1 and 2 of the numerical study presented in section 3 indicate that there is a very interesting connection between the topology of the level sets for the active scalar in the region of initially evolving strong gradients and the formation of strong nonlinear and potentially singular fronts. In case 1 with the initial data in (3.1), the developing region with large gradients for θ impinges on a hyperbolic saddle point in the scalar level sets and in section 3.2, we carefully documented subsequent strongly nonlinear behaviour with a potentially singular thermal front forming in finite time. In case 2 with the initial data in (3.2), the developing region with large gradients for θ impinges on an elliptic centre in the active scalar level sets and we documented through the diagnostics in section 3.3 that there

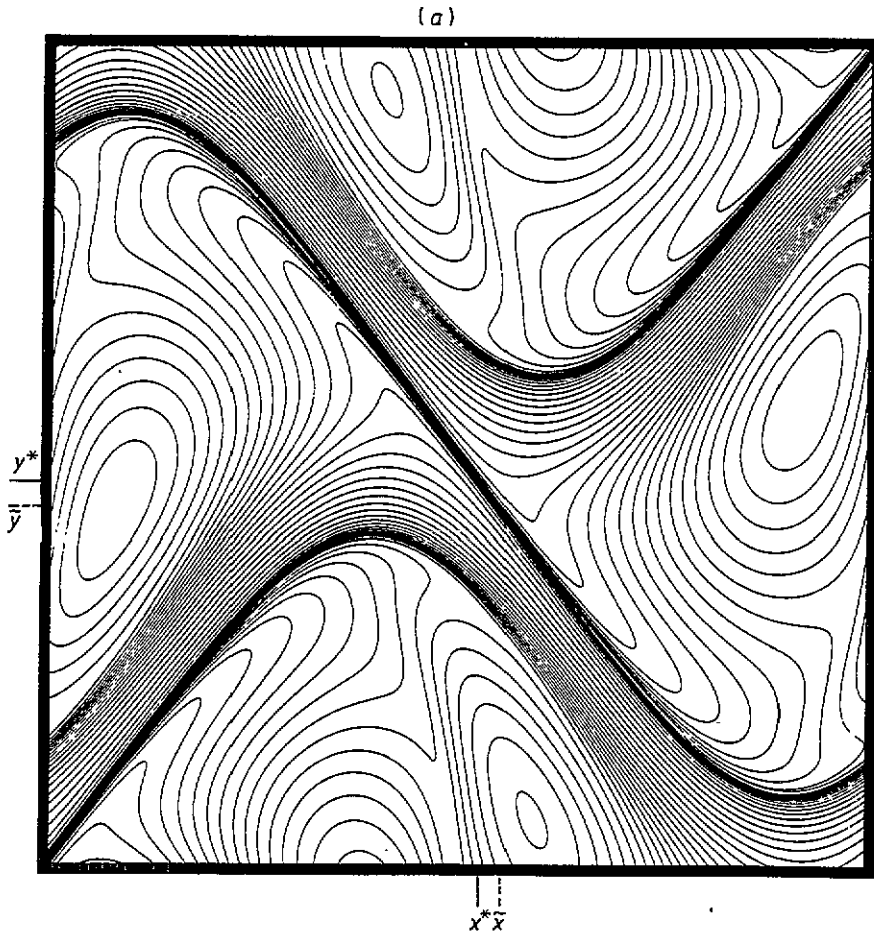


Figure 5. Same as before, at $t = 7.5$. Although the points of maximum gradient and strain appear to have separated slightly since the previous snap-shot, we attribute this to their failure to lie exactly on grid points. (a) Contours of θ . (b) Contours of ψ

is substantial depletion of local nonlinear interaction without the possibility of a singular front forming in finite time. These two examples demonstrate the crucial role of the local topology of level sets in the formation of strong and potentially singular fronts. Here we continue the symbiotic interaction of mathematical theory and numerical simulation utilized throughout this paper by providing an explanation through mathematical analysis of the role of topology of the scalar level sets in strong front formation. Our intention in this section of the paper is to provide an expository account of these matters without technical details—the mathematical details are presented in section 5.

4.1. Classical frontogenesis with trivial active scalar topology is impossible

Classical frontogenesis in geophysical fluid dynamics is the rapid temporal development of a sharp front between warm and cold masses of air. In some simplified semi-geostrophic approximations in meteorology incorporating ageostrophic effects beyond (1.1)–(1.3), the formation of these sharp fronts corresponds to a finite time singularity (see [1] and references there); the physical picture is much like the formation of shock waves in compressible fluid flow [10]. In case 1 from section 3, we presented numerical evidence for the possibility

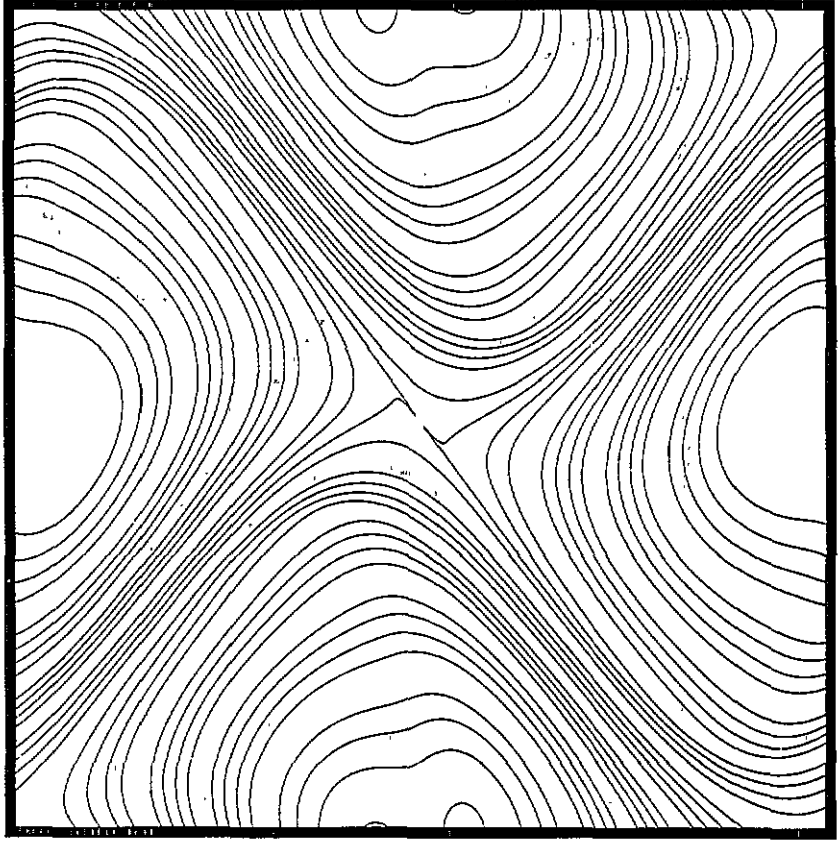


Figure 5. (Continued)

of nonclassical frontogenesis involving fronts with cusps (figures 3–6) completely within the quasigeostrophic approximation and without incorporating any ageostrophic effects; however, a hyperbolic saddle in the scalar topology played a crucial role. Here we study whether classical frontogenesis with trivial topology is possible within the quasigeostrophic equations in (1.1)–(1.3).

For the purposes of exposition, we consider a simplified scenario for classical frontogenesis with trivial topology. To do this, we consider a smooth curve in the plane, the front curve, written as a graph

$$x_2 = f(x_1). \quad (4.1)$$

We consider a smooth function of one variable, $F(s)$ with the properties that $F(s) = 1$ for $s \geq 3$, $F(s) = 0$ for $s \leq 1$ and $F'(s) \geq 0$ for all s . We assume a simplified ansatz for classical frontogenesis with trivial topology where the thermal 2-D quasigeostrophic active scalar has the form

$$\theta(x, t) = F\left(\frac{x_2 - f(x_1)}{\delta(t)}\right) \quad (4.2)$$

where for some critical time, $T_* > 0$

$$\delta(t) \rightarrow 0 \quad \text{as } t \nearrow T_*. \quad (4.3)$$

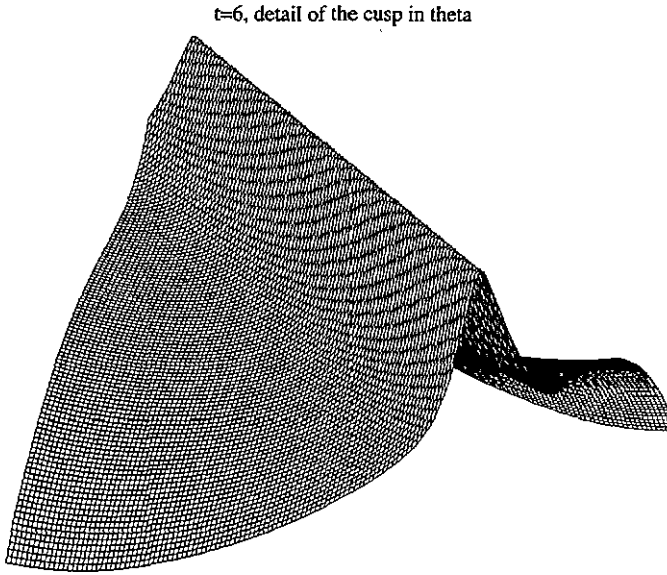


Figure 6. Case 1, $t = 6$. Detail of the cusp developing in θ . The nature of this front differs significantly from the 'shock-like' front of classical frontogenesis. It is analogous though to the configuration with potentially collapsing nearly antiparallel vortex tubes in 3-D Euler.

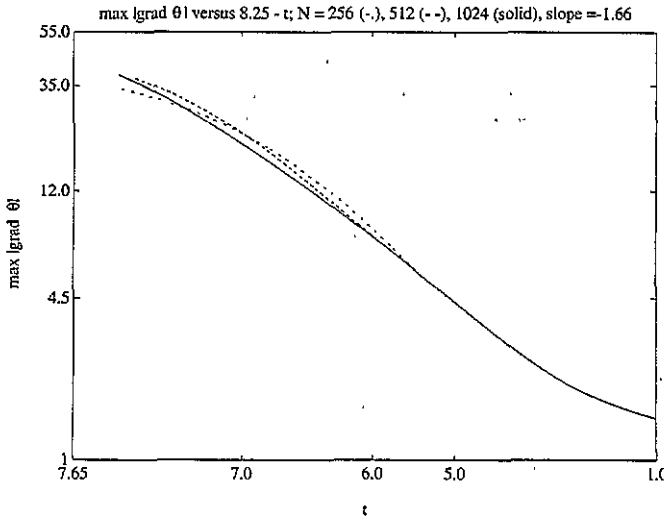


Figure 7. Log-log depiction of the growth of $\max |\nabla\theta|$. Three runs with different resolution are superimposed, showing their tendency to align with a straight line, corresponding to the development of a singularity near $t = 8.25$. The times at which each run departs from this straight line correspond roughly to those at which their resolution fails, at least for computing maxima adequately.

With the properties for the functions, f, F , described above (4.1), the form for the active scalar in (4.2) models classical frontogenesis with trivial level set topology for θ with a potential singularity forming at the time, $t = T_*$. At the time, T_* , the scalar becomes

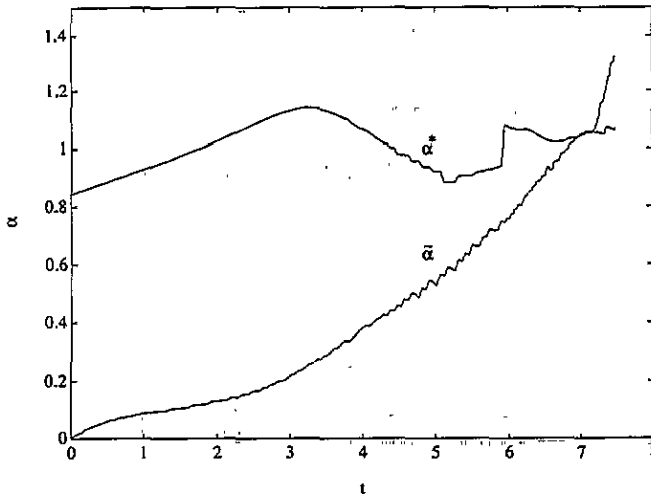


Figure 8. Case 1. Evolution of the strain, computed where it is maximum (α^*) and where the maximum gradient of θ is maximum ($\tilde{\alpha}$). The latter gives a better diagnostic for nonlinear behaviour at the early stages of front formation, when α^* is nearly constant. After the two nearly collide and the grid starts being insufficient for computing maxima and their precise location, however, α^* appears to display nonlinearity more consistently.

discontinuous across the curve $x_2 = f(x_1)$ with different limiting values for the temperature on each side of the front, i.e. classical frontogenesis potentially occurs at $t = T_*$. However, despite this potential singularity formation, the direction field $\xi = \frac{\nabla^{\perp} \theta}{|\nabla^{\perp} \theta|}$ remains smooth throughout this process; in fact, the direction field is time independent and is given explicitly by

$$\xi(x, t) = - \frac{1}{\sqrt{1 + (f'(x_1))^2}} \begin{pmatrix} 1 \\ f'(x_1) \end{pmatrix}. \tag{4.4}$$

In theorem 5.1 of section 5, we state and prove a general theorem with the following intuitive context:

If locally the direction field $\xi(x, t)$ remains smooth
 (in a very weak sense) as $t \nearrow T_*$, then no finite time
 singularity is possible as $t \nearrow T_*$. (4.5)

An immediate corollary of theorem 5.1 is that the classical frontogenesis scenario with trivial topology described in (4.2) and (4.3) above is impossible for any function $\delta(t)$ with $\delta(t) \rightarrow 0$ as $t \nearrow T_*$ since the direction field $\xi(x, t)$ as computed in (4.4) remains smooth on the closed time interval, $0 \leq t \leq T_*$.

4.2. A singular thermal ridge with trivial active scalar topology is impossible

In case 1 from section 3, as documented in figures 3–6, the numerical evidence suggests nonclassical frontogenesis through the formation of a thermal ridge with a critical role for a hyperbolic saddle in the scalar topology. Here we consider the possibility of singular front

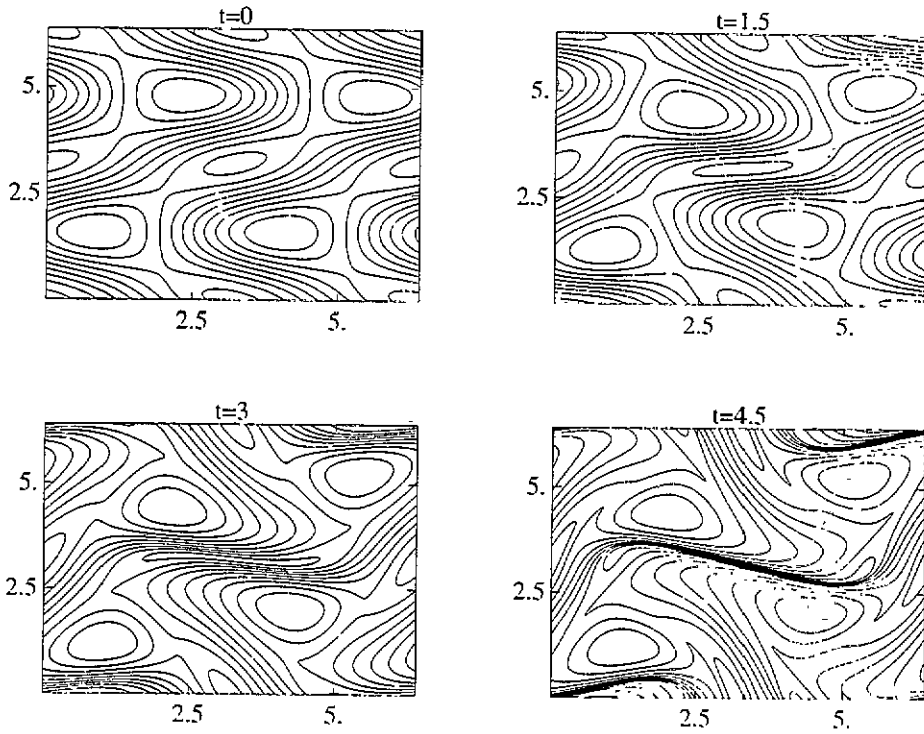


Figure 9. Case 2. Contours of θ between $t = 0$ and $t = 4.5$ showing front formation. In this case, θ has an elliptic point at the centre of the grid. This will exclude the possibility of singular behaviour.

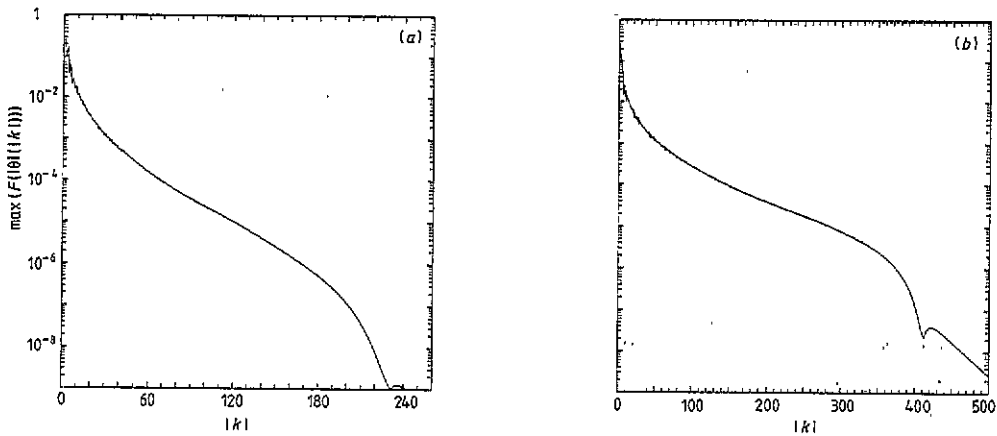


Figure 10. Case 2. Logarithmic plots of the spectrum of theta, averaged over angles. In this case, the decay of energy is exponential, which seems to exclude a tendency toward singular behaviour. The front itself is not as clearly marked as in case 1. We switched from a grid with 512×512 points to one with 1024×1024 at $t = 4$. (a) $t = 4$, front near $|k| = 230$. (b) $t = 5$, front near $|k| = 400$.

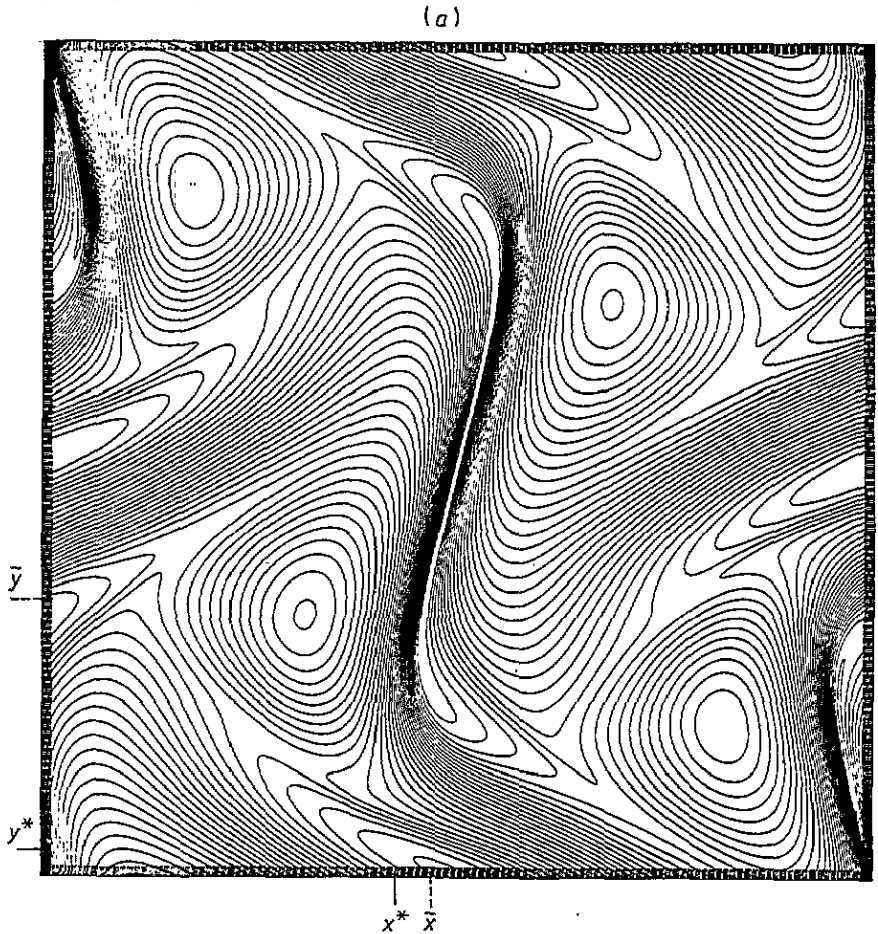


Figure 11. Case 2. Snap-shots of θ at $t = 4$ and $t = 5$, exhibiting strong—but not singular—front formation. As time progresses, the configuration looks more and more like that of a pair of perfectly antiparallel vortex lines, since there is no saddle in θ to preserve the two-dimensionality. The points of maximum $|\nabla\theta|$ and α remain at distinct, distant positions. (a) $t = 4$. (b) $t = 5$

formation through a thermal ridge with trivial topology (no hyperbolic saddle, etc) in the scalar level sets.

For the purposes of exposition, as in section 4.1 we consider a simplified scenario. We consider a smooth curve in the plane as described in (4.1) and utilize the same ansatz as in (4.2) so that there is trivial scalar level set topology. However, here we take a completely different profile function, $F(s)$, which corresponds to a thermal ridge. Thus, we assume that $F(s)$ is a non-negative smooth bump function with $F(s)$ identically zero for $s \leq 1$ and for $s \geq 3$, $F'(s) > 0$ for $1 < s < 2$, and $F'(s) < 0$ for $2 < s < 3$. With this choice of F and the ansatz in (4.2), as t converges to the candidate singular time, T_* , the solution looks like a thermal ridge as in figure 6 from section 3 with the crucial difference that the level set topology for θ is completely trivial here. In contrast to the case studied in section 4.1, as $t \nearrow T_*$ the direction field $\xi(x, t) = \frac{\nabla^\perp \theta}{|\nabla^\perp \theta|}$ is no longer smooth in the limit, in fact the direction field is discontinuous at the limiting time, $t = T_*$, and is given by

(b)

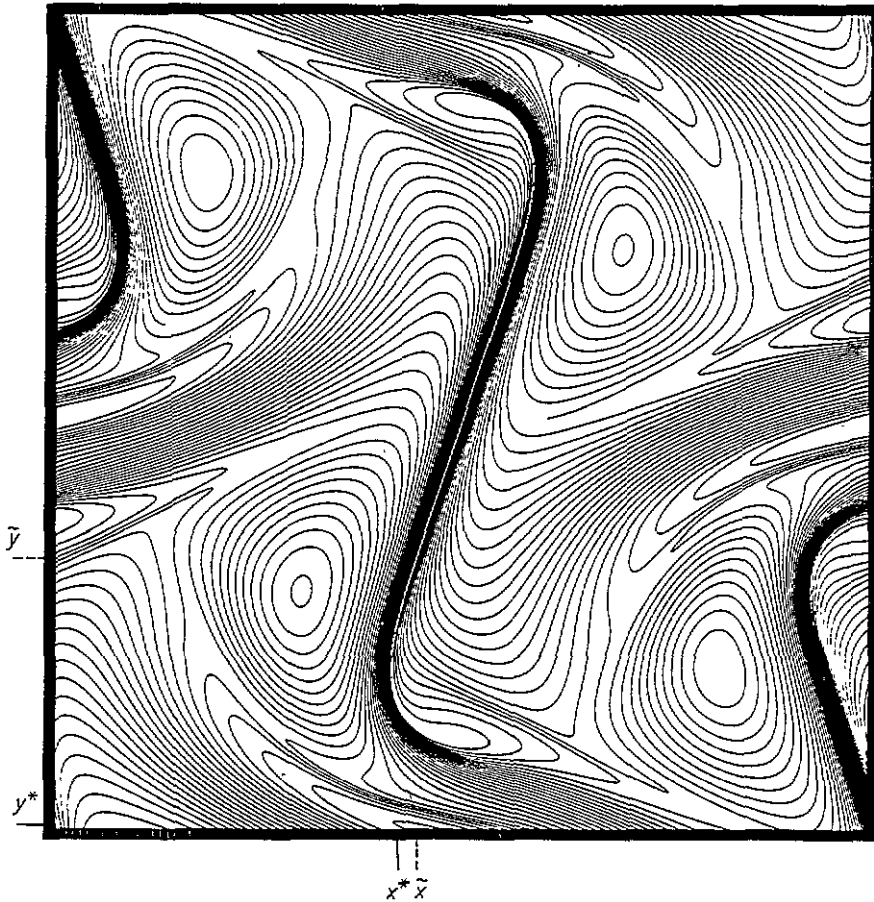


Figure 11. (Continued)

$$\xi(s) = \text{sign}(x_2 - f(x_1)) \frac{1}{\sqrt{1 + (f'(x_1))^2}} \begin{pmatrix} 1 \\ f'(x_1) \end{pmatrix}. \tag{4.6}$$

This behaviour with a discontinuous limiting direction field as $t \nearrow T_*$, with the ansatz in (4.1) and (4.2) is a special example of what we call *regularly directed* behaviour in section 5. In theorem 5.2 of section 5, we prove a result which guarantees that no singularities in finite time are possible for regularly directed limiting behaviour in a very precise sense. In particular, at the end of section 5, we present detailed calculations which verify this theorem for the thermal ridges described in this section. Thus, the mathematical theory in section 5 implies that

thermal ridges with trivial level set topology as described in this section can never become singular in a finite time, T_* for any arbitrary scaling function $\delta(t)$ with $\delta(t) \downarrow 0$ as $t \rightarrow T_*$. (4.7)

4.3. Detailed behaviour of level sets in cases 1 and 2

Here with the theoretical facts mentioned in sections 4.1 and 4.2, we examine the behaviour of the level sets of the active scalar in more detail for the numerical solutions with the

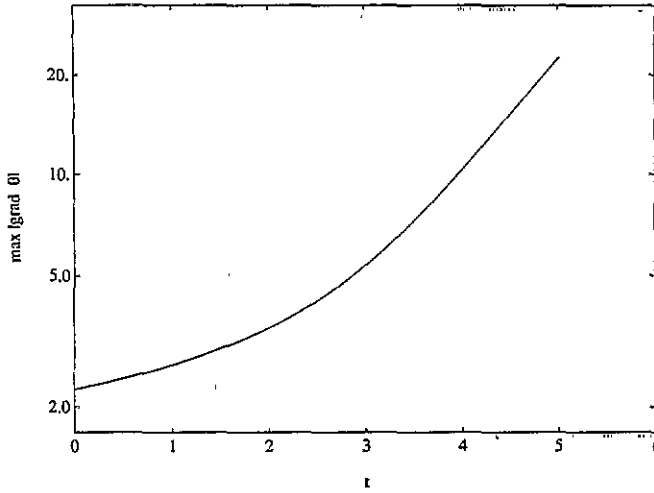


Figure 12. Case 2. Logarithmic plot of the growth of $\max |\nabla\theta|$. Notice the fast convergence to a straight line, corresponding to exponential growth.

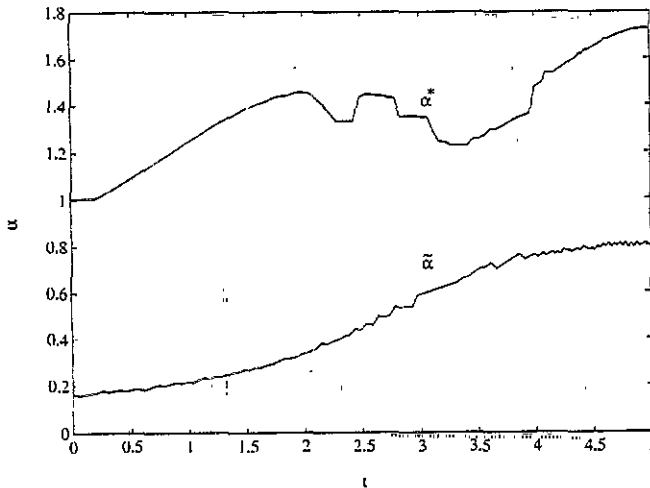


Figure 13. Case 2. Evolution of α^* and $\tilde{\alpha}$. As the locations with maximum gradients and strains remain clearly distinct, the corresponding values of α do not meet, nor does either show strongly nonlinear growth.

initial data for case 1 and case 2 from sections 3.2 and 3.3 respectively. For case 1 with the initial data in (3.1), in figures 16 and 17, we plot the evolution of selected equispaced level sets for the active scalar at the times, $t = 0, 4, 6$.

The plots in figure 16(a, b, c) involve eleven equispaced contours on the outside of the hyperbolic saddle as time evolves while those in figure 17(a, b, c) involve equispaced evolving contours inside the hyperbolic saddle. In order to contrast the behaviour in these two different situations, in figures 18 and 19, we present similar plots for the initial data for case 2 in (3.2) at the times $t = 0, 3$, and 4.5 where the initial nonlinear development impinges on an elliptic centre—the boundaries of the contours in this case extend outside

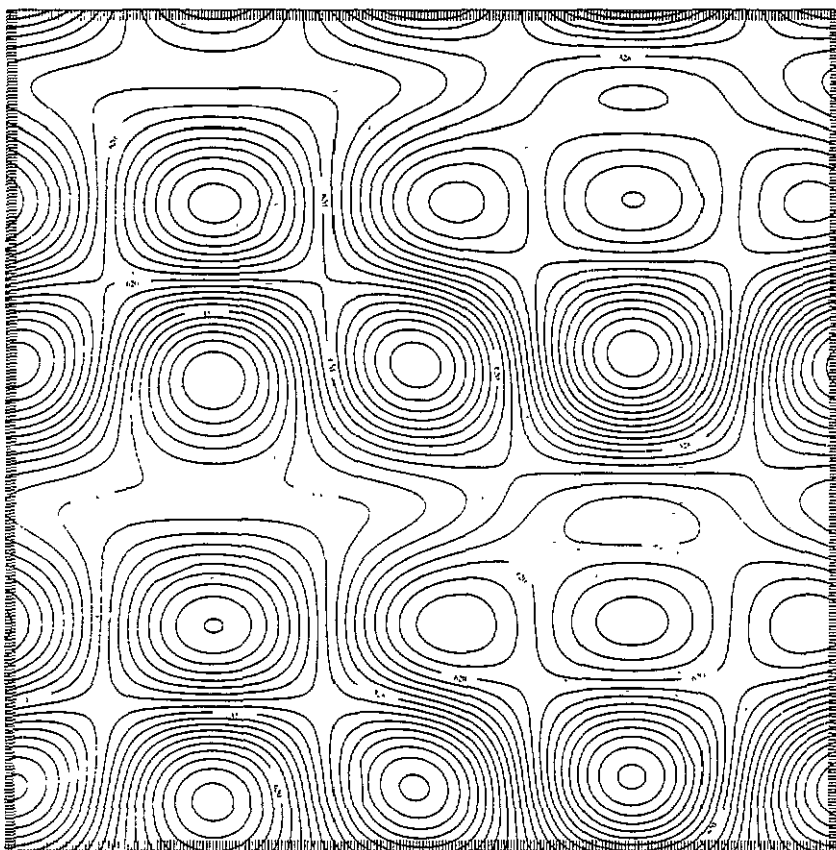


Figure 14. Case 3. Initial condition, taken as representative of a 'general' large scale flow.

(figure 18) and inside (figure 19) the two heteroclinic stream lines which connect two distant hyperbolic saddles and enclose the elliptic centre in the scalar level sets.

It is evident from the plots in figures 18 and 19 that for case 2 with the strong gradient region impinging on an elliptic centre, the packing of level sets in the region near the elliptic centre is almost completely one-dimensional. This behaviour is also evident in the temperature contour plots for this case presented earlier in figure 11(*a, b*). With this numerical evidence it is clear that the contours near the elliptic centre behave like the thermal ridge theoretical example discussed earlier in section 4.2. According to theorem 5.2, no finite time singularities can occur in a region with the trivial level set topology in the thermal ridge and indeed our refined numerical diagnostics in figures 12 and 13 for case 2 confirm that strong nonlinearity has been depleted in this geometric configuration.

In contrast, the detailed behaviour of the level sets for case 1 depicted in figures 16, 17 where the region of strong gradients impinges on a hyperbolic saddle is quite different. It is evident from figures 16(*b*) and 17(*b*) that at time $t = 4$ strong gradients in θ are created which definitely are not quasi-one-dimensional because a two-dimensional behaviour is always driven by the hyperbolic saddle in the temperature field which necessarily persists for all time. This behaviour for the level sets with nontrivial topology involving a hyperbolic saddle is confirmed by the detailed diagnostics in figures 7 and 8 which give evidence for strongly nonlinear and potentially singular behaviour in case 1. However, our present mathematical theory is unable to answer whether a finite time singularity actually occurs in

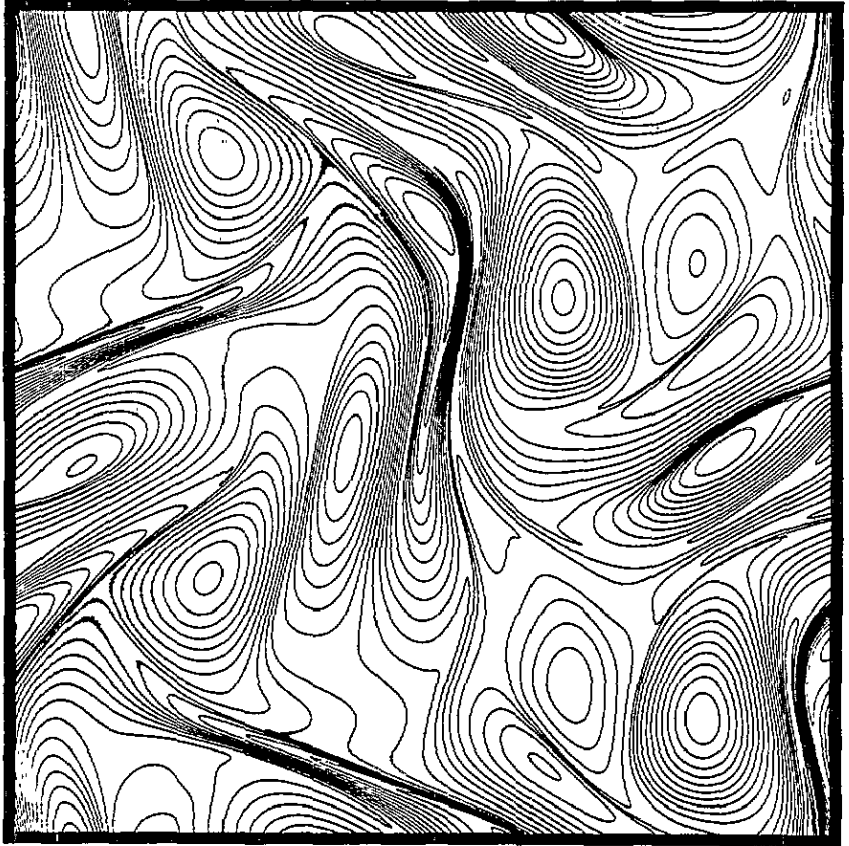


Figure 15. Case 3, $t = 3$. Elongated fronts have formed at various locations. A detailed study of the evolution of these fronts would require the use of grids with a prohibitively small mesh size. This slightly under-resolved computation, however, should suffice to show that the strong development of fronts is inherent to the equations, occurring for a wide range of initial data.

case 1 or whether this is simply a strongly nonlinear but nonsingular event.

To summarize, the rigorous theorems mentioned in sections 4.1 and 4.2 above together with the detailed numerical experiments and diagnostics presented here and in section 3 all point to the following general principle:

If the level set topology in the temperature field for the 2-D
quasigeostrophic active scalar in the region of strong scalar
gradients does not contain a hyperbolic saddle, then no finite
time singularity is possible. (4.8)

Finally, we recall the analogy developed in section 2.2 between the level sets of the thermal active scalar and the vortex lines of a three-dimensional incompressible flow. With this analogy, both case 1 and case 2 as well as the thermal ridge with trivial topology discussed in section 4.2 correspond to the behaviour of anti-parallel vortex filaments in a 3-D incompressible flow. The behaviour in case 1 corresponds in this analogy to similar but more complex strongly nonlinear and potentially singular behaviour in the anti-parallel pair documented by Kerr [14] in very interesting recent work; on the other hand, the

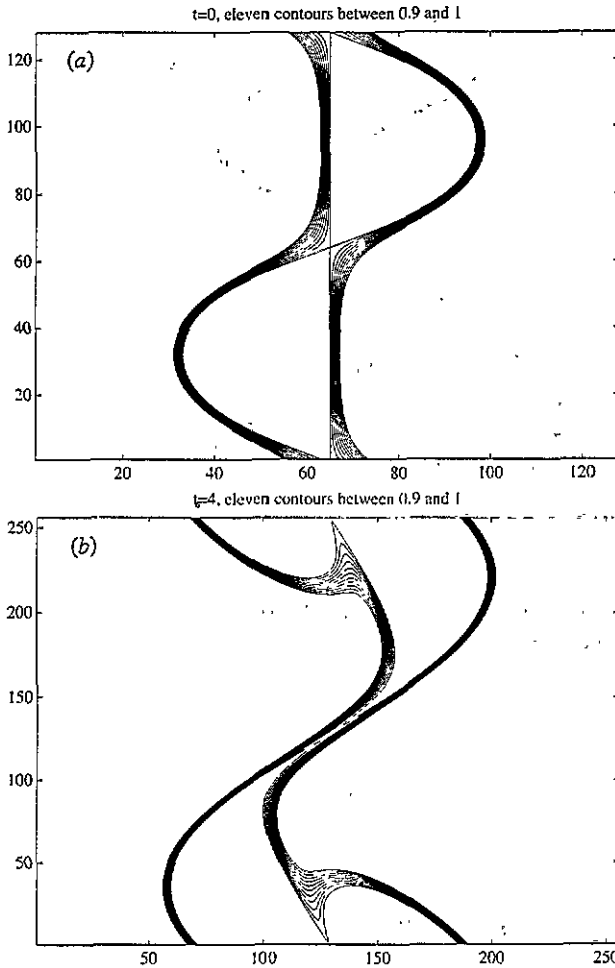


Figure 16. Case 1. Evolution of eleven selected contour lines on the outside of the saddle, showing the preservation of a two-dimensional pattern despite the fast elongation of the fronts. Whether nonlinearity will or not survive depends on a crucial balance between the rate at which the contours are packing and that at which the angle of aperture of the saddle is converging to zero. (a) $t = 0$, a regular saddle point. (b) $t = 4$, start of the stretching of contour lines. (c) $t = 6$, 'mature' front, with densely packed contours and very distorted saddle.

behaviour with different topology documented in case 2 and section 4.2 corresponds to nonsingular behaviour in the antiparallel vortex pair with somewhat different initial data (see the references in [2, 14] for this type of behaviour in 3-D incompressible flow).

5. Analytic and geometric constraints on singular solutions

Here we prove the precise mathematical theorems discussed in sections 4.1 and 4.2. At the end of this section, we apply theorem 5.2 to the thermal ridge scenario described in section 4.2.

5.1. Precise statement of results

We consider a QG active scalar $\theta(x, t)$ with smooth initial data and suppose the scalar is

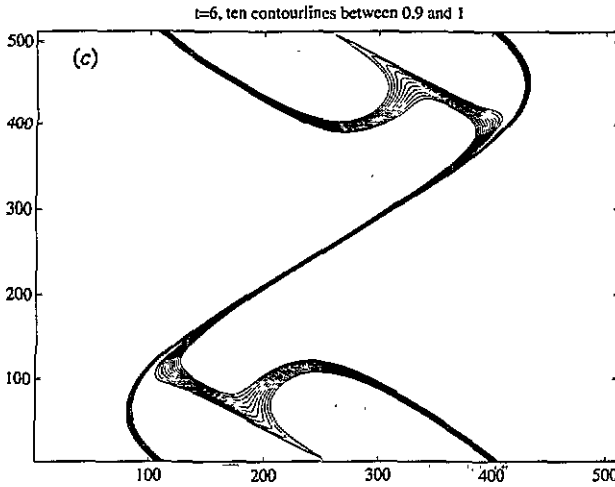


Figure 16. (Continued)

defined and smooth for $(x, t) \in \mathbb{R}^2 \times [0, T)$. Recall from (2.31) the particle trajectories $X(q, t)$, which are solutions of

$$\frac{dX}{dt} = v(X, t)$$

Also recall that $\xi = \frac{\nabla \theta}{|\nabla \theta|}$ is the direction field tangent to the level sets. We say that a set Ω_0 is *smoothly directed* if there exists $\rho > 0$ such that

$$\sup_{q \in \Omega_0} \int_0^T |v(X(q, t), t)|^2 dt < \infty \tag{5.1a}$$

$$\sup_{q \in \Omega_0^*} \int_0^T \|\nabla \xi(\cdot, t)\|_{L^\infty(B_\rho(X(q, t)))}^2 dt < \infty \tag{5.1b}$$

where $B_\rho(X)$ is the ball of radius ρ centred at X and

$$\Omega_0^* = \{q \in \Omega_0; |\nabla \theta_0(q)| \neq 0\} .$$

If Ω_0 is a set we denote by Ω_t its image at time t under the particle trajectory map

$$\Omega_t = X(\Omega_0, t)$$

and by $\mathcal{O}_T(\Omega_0)$ the semi-orbit:

$$\mathcal{O}_T(\Omega_0) = \{(x, t) | x \in \Omega_t, 0 \leq t \leq T\}$$

Theorem 5.1. Assume Ω_0 is smoothly directed. Then

$$\sup_{\mathcal{O}_T(\Omega_0)} |\nabla \theta(x, t)| < \infty .$$

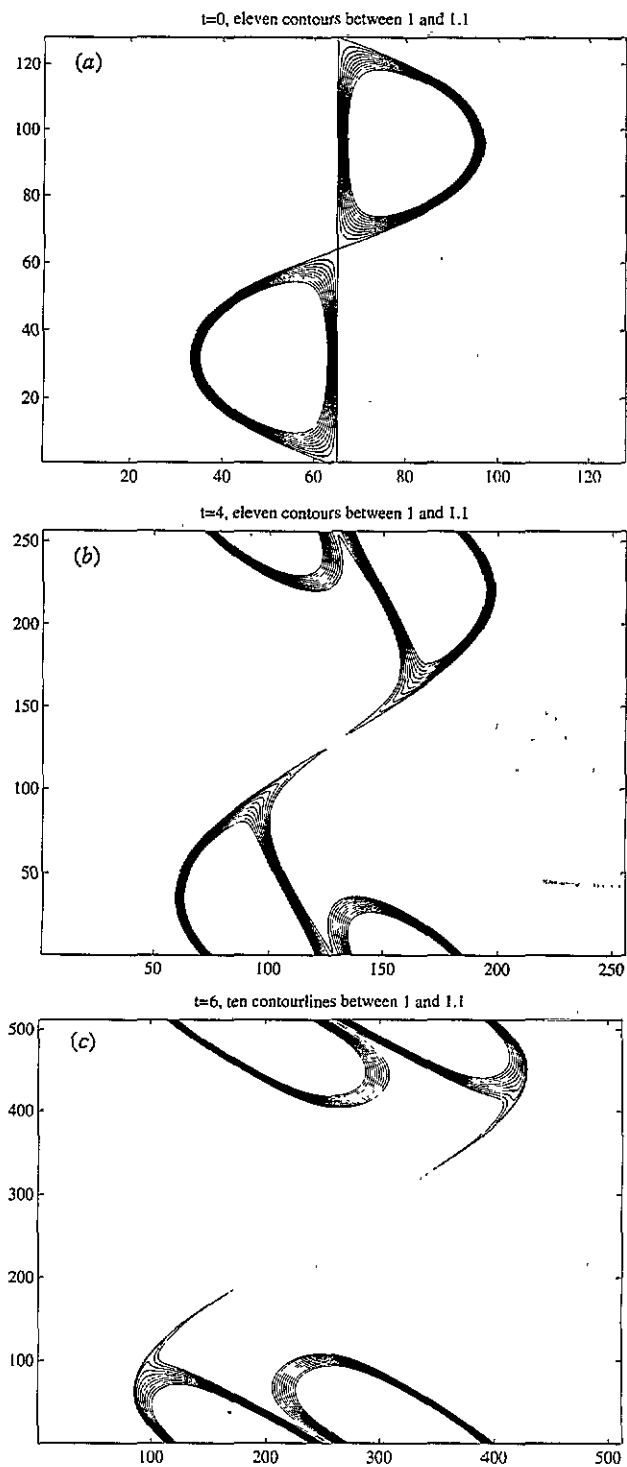


Figure 17. Case 1. Evolution of eleven contours inside the saddle, showing the survival of nontrivial topology for all times. (a) $t = 0$. (b) $t = 4$. (c) $t = 6$.

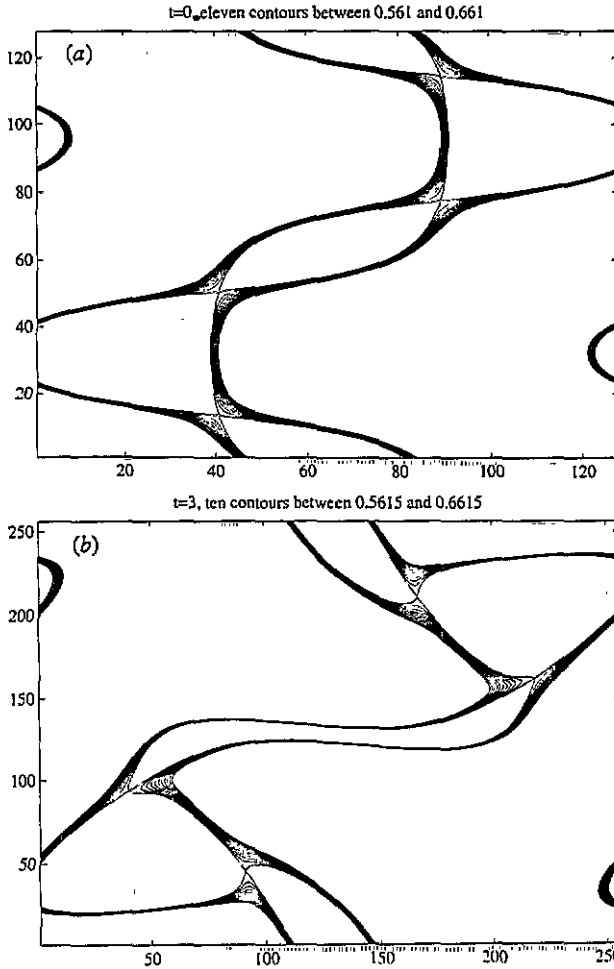


Figure 18. Case 2. Evolution of eleven contours on the outside of the saddles between which the elliptic region is being crushed. (a) $t = 0$. (b) $t = 3$. (c) $t = 4.5$. Near the centre of the grid, where the gradients are largest, the configuration looks purely one-dimensional, the analogue of two perfectly parallel vortex lines.

i.e. if the direction field is smooth locally on a set moving with the fluid in the precise sense of (5.1b), then no singularity is possible in that set.

Next we state a general technical theorem which applies to the prototypical situation in section 4.2 where the direction field is not smooth but the special structure of the singular integral operators allows depletion of nonlinearity on special geometric configurations. Related results for the 3-D Euler equations are presented in [6] and [9]. We say that the set Ω_0 is regularly directed if there exists $\rho > 0$ such that

$$\sup_{q \in \Omega_0^*} \int_0^T K_\rho(X(q, t)) dt < \infty \tag{5.2}$$

where

$$K_\rho(x) = \int_{|y| \leq \rho} |\hat{y} \cdot \xi^\perp(x)| |\xi^\perp(x) \cdot \xi(x+y)| A(x+y) \frac{dy}{|y|^2}. \tag{5.3}$$

In (5.3) and elsewhere in this section, we define $A(x)$ to be $A(x) = |\nabla^\perp \theta|$.

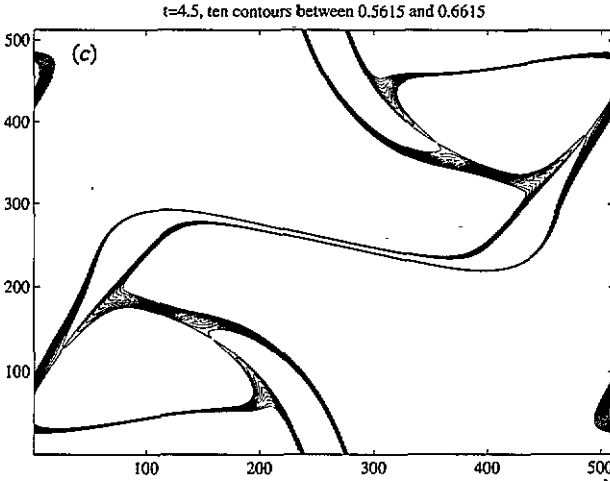


Figure 18. (Continued)

Theorem 2. Assume that Ω_0 is regularly directed. Then

$$\sup_{\partial_T(\Omega_0)} |\nabla\theta(x, t)| < \infty$$

i.e. if a set moving with the fluid is regularly directed, there is depletion of nonlinearity and no singularity is possible on that set.

5.2. The proofs of the theorems

The proofs of both theorems rely on special formulae for the level set stretching factor, α , from (2.15), (2.16) together with a local version of the proof that we utilized in theorem 2.1 to demonstrate that (3) implies (2). We start by computing the full gradient of the velocity field v from the formula in (2.8).

$$(\nabla v)(x) = -\nabla_x \int \frac{1}{|y|} (\nabla^\perp \theta)(x + y) dy$$

Differentiating under the integral sign we get

$$(\nabla v)(x) = - \int \frac{1}{|y|} (\nabla_y \nabla_y^\perp \theta)(x + y) dy .$$

We write the integral as a limit as $\epsilon \rightarrow 0$ of integrals on $|y| > \epsilon$. Because the two gradients applied to θ commute, we can choose any one of them and integrate by parts. The limit of the contributions from $|y| = \epsilon$ vanishes. In this fashion, we obtain two formulae:

$$(\nabla v)(x) = -P.V. \int (\hat{y}^\perp \otimes (\nabla\theta(x + y))) \frac{dy}{|y|^2} \tag{5.4}$$

and

$$(\nabla v)(x) = -P.V. \int ((\nabla^\perp \theta(x + y)) \otimes \hat{y}) \frac{dy}{|y|^2} . \tag{5.5}$$

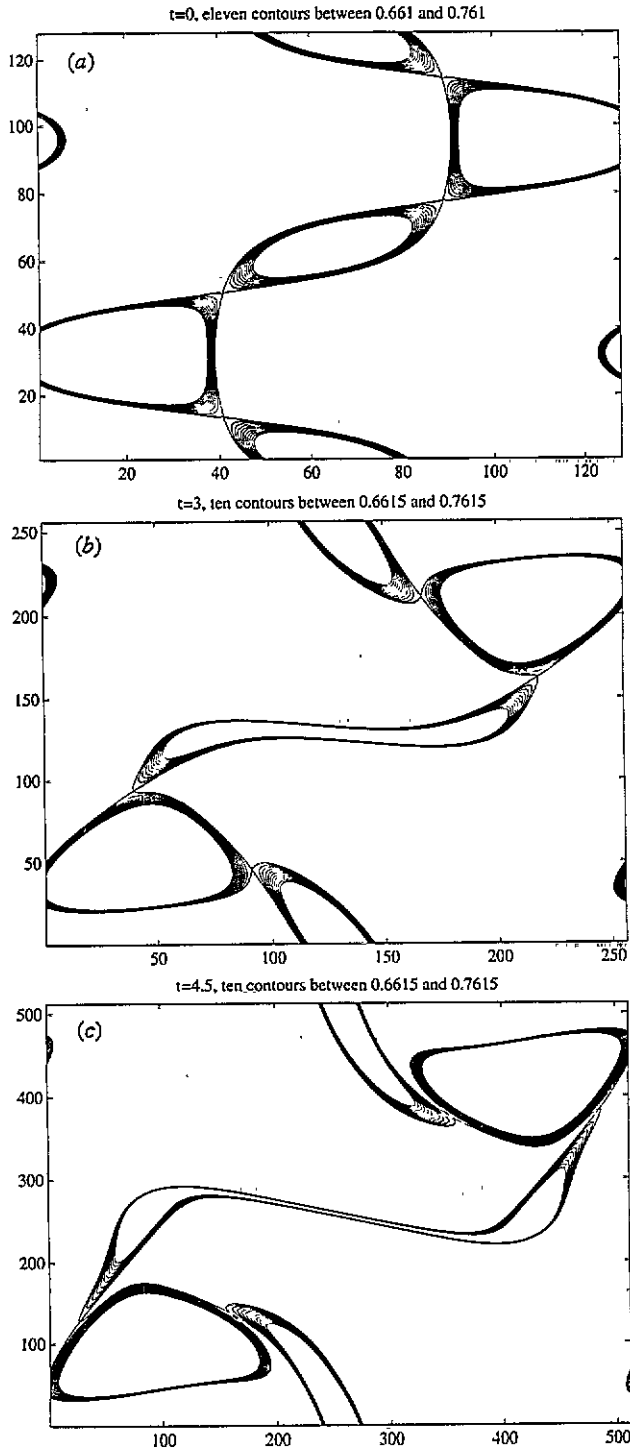


Figure 19. Case 2. Eleven contours inside the saddles surrounding the elliptic region. The configuration at the centre of the grid converges to the regularly-directed scenario. (a) $t = 0$. (b) $t = 3$. (c) $t = 4.5$.

Writing

$$\nabla^\perp \theta = A\xi$$

and using the definition from (2.4) and (2.15) that

$$\alpha(x) = (((\nabla v)(x))\xi(x)) \cdot \xi(x)$$

we deduce the two representations of α

$$\alpha(x) = +P.V. \int ((\hat{y} \cdot \xi^\perp(x))(\xi(x+y) \cdot \xi^\perp(x))) A(x+y) \frac{dy}{|y|^2} \tag{5.6}$$

and

$$\alpha(x) = -P.V. \int (((\hat{y} \cdot \xi(x))(\xi(x+y) \cdot \xi(x)))A(x+y) \frac{dy}{|y|^2} . \tag{5.7}$$

Let us consider now a number $\rho > 0$ and decompose

$$\alpha(x) = \alpha_{in}(x) + \alpha_{out}(x)$$

where

$$\alpha_{in}(x) = P.V. \int \chi\left(\frac{|y|}{\rho}\right) \dots$$

and

$$\alpha_{out}(x) = P.V. \int \left(1 - \chi\left(\frac{|y|}{\rho}\right)\right) \dots$$

with $\chi(r)$ a smooth non-negative function of one positive variable satisfying $\chi(r) = 1$ for $0 \leq r \leq \frac{1}{2}$, $\chi(r) = 0$ for $r \geq 1$.

It is easy to prove the estimate:

$$|\alpha_{out}(x)| \leq C\rho^{-2} \|\theta\|_{L^2} . \tag{5.8}$$

Indeed using any of the two representations, the fact that $A\xi = \nabla^\perp \theta$ and integrating by parts one obtains

$$|\alpha_{out}(x)| \leq C\rho^{-1} \int_{|y| \geq \frac{1}{2}\rho} |\theta(x+y)| \frac{dy}{|y|^2} .$$

Let us consider now the situation in which the direction field ξ is smooth in the ball of centre x and radius ρ , corresponding to the smoothly directed case. We use the representation in (5.6). Let us denote by G the maximum of the gradient of ξ there:

$$G = \sup_{|y| \leq \rho} |\nabla \xi(x+y)| .$$

Clearly

$$|\xi(x + y) \cdot \xi^\perp(x)| \leq G|y|$$

for $|y| \leq \rho$. We deduce from (5.6) that

$$|\alpha_{in}(x)| \leq G \int \chi \left(\frac{|y|}{\rho} \right) A(x + y) \frac{dy}{|y|}.$$

Now we use the fact that

$$A = \xi \cdot (\nabla^\perp \theta)$$

and integrate by parts:

$$\int \chi \left(\frac{|y|}{\rho} \right) A(x + y) \frac{dy}{|y|} = - \int \theta(x + y) \nabla_y^\perp \cdot \left(\xi(x + y) \chi \left(\frac{|y|}{\rho} \right) \frac{1}{|y|} \right) dy.$$

We carry out the differentiation and obtain three terms which we denote I, II and III:

$$I = - \int (\nabla_y^\perp \cdot \xi(x + y)) \theta(x + y) \chi \left(\frac{|y|}{\rho} \right) \frac{dy}{|y|}$$

$$II = - \int \theta(x + y) \xi(x + y) \cdot \nabla_y^\perp \left(\chi \left(\frac{|y|}{\rho} \right) \right) \frac{dy}{|y|}$$

and

$$III = P.V. \int (\xi(x + y) \cdot \hat{y}^\perp) \theta(x + y) \chi \left(\frac{|y|}{\rho} \right) \frac{dy}{|y|^2}$$

The first two can be estimated in a straightforward manner:

$$|I| \leq C\rho G \|\theta\|_{L^\infty}$$

and

$$|II| \leq C \|\theta\|_{L^\infty}.$$

We write in the third term $\xi(x + y) = \xi(x) + (\xi(x + y) - \xi(x))$ and therefore

$$III = \xi(x) \cdot P.V. \int \hat{y}^\perp \theta(x + y) \frac{dy}{|y|^2} + III'$$

with

$$|III'| \leq C (\rho G \|\theta\|_{L^\infty} + \rho^{-1} \|\theta\|_{L^2}).$$

We observe that

$$P.V. \int \hat{y}^\perp \theta(x + y) \frac{dy}{|y|^2} = -v(x) \tag{5.9}$$

thus

$$|\alpha_{in}(x)| \leq CG [|v(x)| + (\rho G + 1) \|\theta\|_{L^\infty} + \rho^{-1} \|\theta\|_{L^2}]. \tag{5.10}$$

Combining this with the estimate in (5.8) we proved:

Lemma 5.1. Assume that x is such that

$$G := \sup_{|y| \leq \rho} |\nabla \xi(x + y)|$$

and $|v(x)|$ are finite. Then $|\alpha(x)|$ is bounded by

$$|\alpha(x)| \leq C[G|v(x)| + (\rho G + 1)(G\|\theta\|_{L^\infty} + \rho^{-2}\|\theta\|_{L^2})].$$

Proof of theorem 5.1. If Ω_0 is smoothly directed then we can apply lemma 1 with $x = X(q, t)$, for any $q \in \Omega_0$ and any $t \in [0, T]$. Using the ordinary differential equation from (2.15), (2.32),

$$\frac{d}{dt} |\nabla^\perp \theta(X(q, t), t)| = \alpha(X(q, t), t) |\nabla^\perp \theta(X(q, t), t)|$$

and the bound in lemma 1 we obtain

$$\sup_{\mathcal{O}_T(\Omega_0)} |\nabla \theta(x, t)| \leq e^Q \sup_{\Omega_0} |\nabla \theta_0|$$

where

$$Q = C \sup_{q \in \Omega_0} \int_0^T E(t) dt$$

$$E(t) = [G(x)|v(x)| + (\rho G(x) + 1)(G(x)\|\theta_0\|_{L^\infty} + \rho^{-2}\|\theta_0\|_{L^2})]$$

$$x = X(q, t)$$

and

$$G(x) = \sup_{B_\rho(x)} |\nabla \xi|.$$

This completes the proof of theorem 5.1. In the above, we used the fact that $\|\theta\|_{L^2}^2(t) = \|\theta_0\|_{L^2}^2$ for all times, t . The proof for theorem 5.2 is simpler and follows directly from the identity for $\alpha(x)$ in (5.6) together with (5.8).

Lemma 5.2. Consider a point $x \in \mathbb{R}^2$ and assume that there exists $\rho > 0$ such that

$$K_\rho(x) = \int_{|y| \leq \rho} |\hat{y} \cdot \xi^\perp(x)| |\xi^\perp(x) \cdot \xi(x + y)| A(x + y) \frac{dy}{|y|^2} < \infty.$$

Then

$$|\alpha(x)| \leq K_\rho(x) + \rho^{-2} \|\theta\|_{L^2} \tag{5.11}$$

The proof of the lemma follows immediately from (5.6) and (5.9). The proof of theorem 5.2 now follows from lemma 2 as the proof of theorem 1 followed from lemma 1. Note that because $\xi(x + y)|A(x + y)| = \nabla^\perp \theta(x + y)$ there is no contribution to the integral from points where $A(x + y) = 0$.

Proof that the thermal ridge from 4.2 is regularly directed. We check that the smooth ridge is regularly directed. Thus, we consider a smooth function $x_2 = f(x_1)$ and a ridge profile F as described in section 4.2 and form

$$\theta(x_1, x_2, t) = F\left(\frac{x_2 - f(x_1)}{\delta(t)}\right).$$

We fix x with $|\nabla^\perp \theta(x)| \neq 0$, choose $\rho = \mathcal{O}(1)$ and estimate $K_\rho(x)$. We note that for any point $z = (z_1, z_2)$ with $A(z) \neq 0$ we have

$$\xi(z) = \pm \frac{1}{\sqrt{1 + (f'(z_1))^2}} \begin{pmatrix} 1 \\ f'(z_1) \end{pmatrix}$$

The sign is decided by which side of the ridge z belongs to. Irrespective of this jump however,

$$|\xi^\perp(x) \cdot \xi(x + y)| \leq \Gamma |y_1|$$

with $\Gamma = \sup |f''|$. The bound

$$A(x + y) \leq \frac{C}{\delta}$$

is obvious and unavoidable. Now the term $|\hat{y} \cdot \xi^\perp(x)|$ is bounded by 1, but also by

$$|\hat{y} \cdot \xi^\perp(x)| \leq C \left[\frac{\delta}{|y|} + \Gamma |y| \right].$$

Indeed, this term is bounded by

$$\frac{1}{|y|} |y_2 - y_1 f'(x_1)|$$

and using the fact that both x and $x + y$ must be in the support of A we have

$$\begin{aligned} |y_2 + x_2 - f(x_1 + y_1)| &\leq C\delta \\ |x_2 - f(x_1)| &\leq C\delta \end{aligned}$$

and hence

$$|y_2 - y_1 f'(x_1)| \leq |f(x_1 + y_1) - f(x_1) - y_1 f'(x_1)| + C\delta.$$

Let us break the integral defining $K_\rho(x)$ in two pieces: the contributions from $|y| \leq \delta$ and those from $|y| \geq \delta$. In the first piece we use polar coordinates and obtain easily a bound

$$\frac{C}{\delta} \int_0^\delta \frac{dr}{r} \Gamma r = C\Gamma$$

The outside piece is not suited for polar coordinates; there we use the fact that for a given y_1 the strip of allowed y_2 , $\Sigma(y_1)$, has width of order $C\delta$ and obtain a bound

$$\frac{C}{\delta} \int_\delta^\rho dy_1 \int_{\Sigma(y_1)} dy_2 \frac{1}{|y|^2} \left(\frac{\delta}{|y|} + \Gamma |y| \right) \Gamma |y_1|$$

It follows thus that

$$K_\rho(x) \leq C\Gamma(1 + \rho\Gamma)$$

which verifies that the smooth ridge is regularly directed. Obviously, if Γ is a function of time which diverges at the time of blow-up, for instance if the front itself forms a corner or a cusp, then the possibility of a finite time singularity is not precluded by this argument.

Acknowledgments

We thank Weinan E for his help and advice regarding the numerical methods from [12, 13]. We also thank Charles Fefferman and Pedro Embid for several perceptive comments and suggestions regarding some of the proofs presented in this paper. The high resolution calculations with $(1024)^2$ Fourier modes were performed at the N S F Pittsburgh Supercomputer Center on a Cray C90. PC was partially supported by grants NSF DMS-9207080 and DOE DE-FG02-92ER25119; AJM was partially supported by grants NSF DMS-99301094, ARO DAAL03-92-G-0010, ONR N00014-89-J-1044.P00003 and DARPA N00014-92-J-1796; ET was partially supported by grants NSF DMS 99301094 and DARPA N00014-92-J-1796.

References

- [1] Pedlosky J 1987 *Geophysical Fluid Dynamics* (New York: Springer) pp 345–68 and 653–70
- [2] Majda A 1991 Vorticity, turbulence, and acoustics in fluid flow *SIAM Rev.* **33** 349–82
- [3] Blumen W 1978 Uniform potential vorticity flow, Part I. Theory of wave interactions and two-dimensional turbulence *J. Atmos. Sci.* **35** 774–83
- [4] Pierrehumbert R T, Held I M and Swanson K 1994 Spectra of local and nonlocal two dimensional turbulence *Chaos, Solitons, and Fractals* in press
- [5] Held I M, Pierrehumbert R T, Garner S and Swanson K 1994 Surface quasigeostrophic dynamics *preprint*
- [6] Constantin P 1994 Geometric statistics in turbulence *SIAM Rev.* **36** 73–98
- [7] Constantin P, Majda A, and Tabak E 1994 Singular front formation in a model for quasigeostrophic flow *Phys. Fluids* **6** (1) 9–11
- [8] Beale J T, Kato T and Majda A 1984 Remarks on breakdown of smooth solutions for the three-dimensional Euler equations *Commun. Math. Phys.* **94** 61–6
- [9] Constantin P, Fefferman C and Majda A 1994 Geometric constraints on potential singularity formation in the 3-D Euler equations, in preparation
- [10] Majda A 1984 Compressible fluid flow and systems of conservation laws in several space variables *Appl. Math. Sci.* **53** (New York: Springer)
- [11] Ponce G 1985 Remarks on a paper by J T Beale, T Kato, and A Majda *Commun. Math. Phys.* **98** 349–56
- [12] E W and Shu C 1993 Effective equations and inverse cascade theory for Kolmogoroff flows *Phys. Fluids* **A** **5** 998–1112
- [13] E W and Shu C 1994 Small-scale structures in Boussinesq convection *Phys. Fluids* **6** (1) 49–58
- [14] Kerr R 1993 Evidence for a singularity of the three dimensional incompressible Euler equations *Phys. Fluids* **A** **6** 1725–39
- [15] Bell J B and Marcus D 1992 Vorticity intensification and transition to turbulence in the three dimension Euler equations *Commun. Math. Phys.* **147** 371–94